



INTERNATIONAL
URANIUM (USA)
CORPORATION

Independence Plaza, Suite 950 • 1050 Seventeenth Street • Denver, CO 80265 • 303 628 7798 (main) • 303 389 4125 (fax)

July 1, 2002

VIA EXPRESS COURIER

Mr. Dan M. Gillen, Branch Chief
Fuel Cycle Licensing Branch
Mail Stop T-8A33
Office of Fuel Cycle Safety and Safeguards
U.S. Nuclear Regulatory Commission
2 White Flint North
11545 Rockville Pike
Rockville, MD 20852-2738

Reference: White Mesa Uranium Mill - Blanding, Utah
International Uranium (USA) Corporation
NRC Source Materials License No. SUA-1358
Docket No. 40-8681

Dear Mr. Gillen:

In accordance with its letter to NRC of March 11, 2002, International Uranium (USA) Corporation ("IUSA") hereby transmits the enclosed report prepared for IUSA by Hydro Geo Chem, Inc., Evaluation of Potential for Seepage of Constituents Present in Alternate Feed Materials Into the Ore Storage Pad, White Mesa Uranium Mill Site, Blanding, Utah (June 28, 2002). The report describes and presents the results of an investigation performed to evaluate the potential for infiltration into the subsurface of water potentially containing constituents found in alternate feed materials which may be temporarily stockpiled on the ore storage pad prior to processing, and the potential for transport of any dissolved constituents originating from the stockpiled materials into the subsurface and/or to perched groundwater. The results of this investigation would be applicable to the Maywood FUSRAP material for which IUSA has requested a license amendment as well as to other alternate feed materials meeting the soil material types described in the

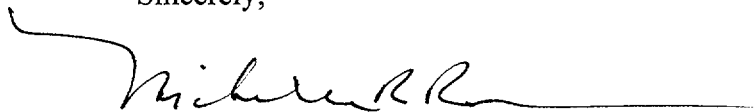
Mr. Dan M. Gillen, U.S. Nuclear Regulatory Commission
July 1, 2002
Page 2 of 2

report, which IUSA has temporarily stockpiled in the past, is currently stockpiling and processing, or may stockpile in the future.

Seepage potential was evaluated by conducting a series of field and laboratory tests as well as sampling and analysis of ore pad materials. These investigations were performed as outlined in our March 11, 2002 letter to the NRC, and as detailed in the enclosed Work Plan – Evaluation of Potential for Infiltration into Ore Pad (May 17, 2002). One notable exception to the Work Plan is that two ring infiltrometer tests (rather than one, as specified in the Work Plan) were performed, together with numerous density tests at randomly selected sample locations, to provide additional data regarding physical properties and the general homogeneity of the ore pad surface.

IUSA hopes that the enclosed report will be useful to the NRC in its review of the Maywood alternate feed amendment request or amendment requests from IUSA for similar potential alternate feed materials. Should you have any questions regarding the information provided, please do not hesitate to contact me at (303) 389-4131.

Sincerely,



Michelle R. Rehmann
Environmental Manager

cc: Ron E. Berg, IUSA
T. Kenneth Miyoshi, IUSA
David C. Frydenlund, IUSA
Ron F. Hochstein, IUSA
Tom Rice, Ute Mountain Ute Tribe
Harold R. Roberts, IUSA
William J. Sinclair, UDEQ
R. William von Till, U.S. Nuclear Regulatory Commission

**EVALUATION OF POTENTIAL FOR SEEPAGE OF
CONSTITUENTS PRESENT IN ALTERNATE FEED
MATERIALS INTO THE ORE STORAGE PAD
WHITE MESA URANIUM MILL SITE
BLANDING, UTAH**

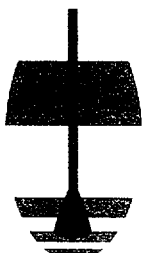
Prepared for:

INTERNATIONAL URANIUM CORPORATION
Independence Plaza, Suite 950
1050 17th Street
Denver, Colorado 80265

Prepared by:

HYDRO GEO CHEM, INC.
51 W. Wetmore, Suite 101
Tucson, Arizona 85705
(520) 293-1500

June 28, 2002



HYDRO GEO CHEM, INC.

Environmental Science & Technology

TABLE OF CONTENTS

1. INTRODUCTION	1
2. SITE DESCRIPTION	3
3. SAMPLE LOCATION AND RATIONALE	5
4. TEST AND SAMPLE COLLECTION METHODS	7
4.1 Nuclear Density/Moisture Tests	7
4.2 Sand Cone Density Tests	7
4.3 Ring Infiltrometer Tests	8
4.4 Sample Collection for Laboratory Analysis	9
5. RESULTS	13
5.1 Ring Infiltrometer Tests	13
5.2 Laboratory Analysis of Permeability	16
5.3 Nuclear Density Tests	17
5.4 Sand Cone Density Tests	17
5.5 Laboratory Analysis of Grain Size Distribution, Moisture Content, Organic Carbon Content, Neutralization Capacity, and Paste pH	18
6. EVALUATION OF POTENTIAL SEEPAGE FROM FEED STOCKPILES ORIGINATING AS PRECIPITATION	21
7. POTENTIAL FOR INFILTRATION OF SEEPAGE FROM FEED STOCKPILES INTO THE ORE STORAGE PAD	25
8. POTENTIAL FOR TRANSPORT OF CONSTITUENTS PRESENT IN FEED STOCKPILES INTO THE SUBSURFACE	29
8.1 Constituents Potentially Present in Feed Stockpiles	30
8.2 Discussion of Behavior of Relatively Conservative Constituents	30
8.3 Retardation of Constituents in the Subsurface	31
8.4 Vapor-Phase Transport	32
8.5 Summary	33
9. CONCLUSIONS	35
10. REFERENCES	37

TABLE OF CONTENTS (continued)

TABLES

1	Ring Infiltration Test Data
2	Evaporation Test Data
3	Vertical Permeability Estimates Based on the Results of Ring Infiltration Tests and Numerical Modeling
4	Laboratory Analysis of Saturated Hydraulic Conductivity
5	Nuclear Field Density Test Results
6	Sand Cone Density Tests
7	Grain Size Distribution
8	Soil Paste pH Measurements
9	Neutralization Capacity and Total Organic Carbon
10	Moisture Content
11	Results of HELP3 Simulations

FIGURES

1	Sample Collection and Test Locations
2	Ring Infiltration Test
3	Nuclear Density Test Performed Near Infiltration Test Location #1
4	Nuclear Density Test Performed at Randomly Selected Sampling Location
5	Attempt to Collect Undisturbed Sample From Compacted Surface of Ore Pad Using a Ring Barrel Sampler
6	Excavation Used for Sample Collection
7	Typical Sand Cone Test
8	Infiltration Location #2

APPENDICES

A	Numerical Modeling of Ring Infiltration Tests
B	Laboratory Analytical Reports
C	Output from HELP3 Simulations

1. INTRODUCTION

This report describes the methods and presents the results of an investigation performed on the ore storage pad at the White Mesa Uranium Mill Site located near Blanding, Utah. The purpose of the investigation was to evaluate: 1) the potential for infiltration into the subsurface of water containing constituents found in alternate feed materials temporarily stored on the ore storage pad prior to processing, and 2) the potential for transport of any dissolved constituents originating from the stockpiled materials into the subsurface and eventually to perched groundwater. For purposes of this evaluation, water potentially infiltrating the ore pad is assumed to originate as pore waters contained in the feeds that are displaced by on-site precipitation that infiltrates the temporarily stockpiled materials and result in seepage into the underlying surface of the ore pad. Incoming feed materials are conservatively assumed to be at their "field capacity" moisture content. Feed materials are stored on the ore pad until enough material is stockpiled for a processing campaign. As a result, the material will be exposed to precipitation for varying periods, but typically up to 2 years. The potential for infiltration of precipitation into stockpiled materials and the potential for seepage of water from these materials was evaluated using HELP3 (Schroeder et al., 1994) using material properties generally characteristic of materials currently stockpiled and anticipated to be stockpiled on the site. Materials that may be stockpiled in the near future include the Maywood FUSRAP material.

The potential for seepage from the stockpiled materials to pass through the surface of the ore pad and for any dissolved metals or organic constituents to be transported into the subsurface was evaluated by conducting a series of field and laboratory tests. These tests were designed to evaluate the uniformity of the ore storage pad surface with regard to the degree of compaction, and to characterize the materials comprising the pad with regard to lithologic characteristics, permeability, and the potential for retardation or immobilization of dissolved organic or metal species that may be present in infiltrating water. Field tests included:

- 1) ring infiltrometer tests,
- 2) sand cone density tests, and
- 3) in-situ density and moisture content tests using a nuclear test gauge.

Samples of ore pad materials were collected for evaluation of:

- 1) moisture content,
- 2) grain size distribution,
- 3) permeability,
- 4) paste pH and neutralization capacity, and
- 5) organic carbon content.

In-situ density and moisture content measurements using a nuclear test gauge were performed by Lambert Associates, Durango, Colorado. Other tests and sample collection were performed by Hydro Geo Chem, Inc. (HGC) personnel with assistance from International Uranium (USA) Corporation (IUSA) personnel.

2. SITE DESCRIPTION

The site is located in southeastern Utah, approximately 6 miles south of Blanding. Precipitation at the site averages less than 11.8 inches, and evapotranspiration exceeds 61 inches annually. The climate is characterized as dry to arid continental (Titan, 1994).

The site is underlain by approximately 5 to 15 feet of fine-grained soils. These are underlain by generally low permeability sandstones that extend to depths of approximately 100 to 120 feet below land surface (bls) at the site, and that host a shallow, naturally low quality, perched water zone. The sandstones are underlain by more than 1,000 feet of very low permeability shales, and sandstones with interbedded, very low permeability materials, that separate the shallow perched water from the regional aquifer, located approximately 1,200 feet bls at the site. In the area of the ore storage pad, depths to the shallow perched water zone are approximately 60 to 70 feet bls at the present time.

The ore storage pad at the site covers a total area of approximately 13 acres. The pad is underlain by compacted, mostly fine-grained material. Crushed limestone was reported to have been incorporated into the pad at the time of construction. The surface of the pad is sloped to promote drainage and prevent off-site movement of drainage.

Feed materials for the Mill are temporarily stockpiled on the ore pad until enough materials are available for a Mill run. The period that materials are stockpiled varies, but is typically about 2 years. Feeds currently stored on site are in piles that typically cover an area of approximately $\frac{1}{10}$ to $1\frac{1}{2}$ acres, and often merge. Pile thicknesses vary but may exceed 30 feet in maximum height. The slopes of the sides of the piles currently on the ore pad vary from approximately 10% to as much as 45%.

3. SAMPLE LOCATION AND RATIONALE

In-situ nuclear density tests were performed at the 39 locations shown in Figure 1. These locations were determined by IUSA based on the use of a random number generator (adjusted when necessary for accessibility) to assure representative coverage. Locations of ring infiltrometer tests and locations where samples were collected for laboratory analysis are also shown in Figure 1. The rationale for the basis of sample location selection is described below.

Nuclear density tests were conducted at 39 randomly selected locations over a large areal extent to provide an estimate of the uniformity of the ore pad surface materials with regard to the degree of compaction, which affects the permeability of the materials. The permeability of a given material will be reduced as the material is more highly compacted. Sand cone density tests were conducted at 5 of the locations (16-15, 18-19, 17-4, 7-4, and 8-10) as an independent test of compaction. Samples for laboratory analysis of moisture content, grain size distribution, permeability (hydraulic conductivity), paste pH, neutralization capacity, and organic carbon content were also collected at these 5 locations. Ring infiltrometer tests were conducted at 2 of the locations (16-15 and 8-10) to independently estimate the vertical permeability. Figures 2 through 8 are photographs showing field performance of some of the testing procedures.

Assuming the ore pad materials have a relatively uniform lithology (which is a reasonable assumption based on the results of the testing), the permeability characteristics of materials at

locations where nuclear density tests were performed but where other tests were not performed can be inferred based on the correlation between the density measurements and permeability test results at locations where both were performed.

4. TEST AND SAMPLE COLLECTION METHODS

The methods used to perform tests and collect and analyze samples during the investigation are described below.

4.1 Nuclear Density/Moisture Tests

In-field nuclear density and moisture content tests were conducted by Lambert Associates, Durango, Colorado, using a nuclear density gauge. Tests were conducted based on the methods described in American Society for Testing of Materials (ASTM) standard methods D2922-96e1 and D3017-96e1. Test locations are shown in Figure 1.

4.2 Sand Cone Density Tests

Sand cone density tests were performed to estimate wet density generally in accordance with ASTM Method D1556-00. Test locations (16-15, 18-19, 17-4, 7-4, and 8-10) are shown in Figure 1. The sand cone test uses a sand funnel apparatus to determine the wet density. The tests consist of: 1) leveling the soil surface and removing loose soil at the test location; 2) excavating a soil sample through the center hole of the template to a depth of approximately 4 inches below land surface; 3) removing and weighing all excavated soil; and 4) determining the weight of the sand required to fill the excavated area and converting the weight of the soil to volume using the density of the

calibrated fine-grained sand. The volume contained in the cone and soil surface template prior to excavation is determined by weighing the sand required to fill the cone when placed on the template. The cone calibration weight is subtracted from the total weight of sand required to fill the hole and cone to obtain the weight and thus the volume of sand in the hole. The volume of the calibrated sand is compared with the wet and dry weights of the excavated material to compute wet and dry density values.

4.3 Ring Infiltrometer Tests

Ring infiltrometer tests were performed at the locations 16-15 and 8-10 as shown in Figure 1. Each test was conducted using a 3.5-foot diameter stainless steel ring equipped with a float valve to maintain a constant water level in the ring, and a graduated supply bottle to measure the rate of water usage. Water levels were maintained at approximately 5 inches. The ring at each test location was inserted as far as possible into the ground surface and the outside of the ring was sealed with bentonite. The hardness of the surface made insertion difficult and the seal somewhat difficult to maintain. Some soaking of the ground surface adjacent to the ring indicating leakage was noted during the tests. Although measures were taken to minimize this leakage by enhancing the bentonite seal, an undetermined amount of leakage did occur, which will result in unavoidable overestimation of infiltration rates.

A concurrent evaporation test was conducted at test location #1 (16-15 on Figure 1) using a 2-foot diameter stainless steel pan of construction and materials similar to that of the ring. Both the ring and the pan are 1 foot in height. Water levels in the pan were measured using a hook gauge sensitive to approximately $1/1,000$ inch. The initial water level in the pan was approximately 5 inches. The evaporation test data were used to correct for ring water usage resulting from evaporation.

Weather conditions were relatively warm and quite windy during performance of both tests. Each test was started in the morning and allowed to run overnight. This allowed time to approach "steady state" conditions during the day so that overnight data could be used for the infiltration rate calculations.

4.4 Sample Collection for Laboratory Analysis

Samples were collected for laboratory analysis of paste pH, neutralization capacity, organic carbon content, grain-size distribution, permeability, and moisture content at the 5 locations shown in Figure 1. At each location, a sample was generally collected from the top few inches, and a sample collected at a depth of 1 to 2 feet below the surface. Samples for analysis of moisture content were collected from the deeper depths at all locations, but only from the surface at 2 locations (7-4 and 8-10). Samples for analysis of permeability were collected only at the surface except at location 8-10, where a sample was also collected at a depth of 2 feet. Excavation for sample collection was generally difficult due to the hard, compacted nature of the materials. Attempts to drive a ring-barrel

sampler into the material were unsuccessful. Excavation for sample collection was typically performed using a backhoe.

Samples for analysis of moisture content were placed in 4-ounce metal cans, sealed with the lid, then further sealed with tape to prevent moisture loss. All other samples were sealed in plastic Ziplock® bags. Each sample was labeled with a date, location, and depth, and placed in a plastic cooler for transport.

Samples collected for moisture content analysis by ASTM Method D.2716 and grain size distribution analysis using sieves and a hydrometer for clay content determination based on ASTM Method D422-63(1990) were shipped to Horizon Labs, in Tucson, Arizona. Samples collected for neutralization capacity and organic carbon content analysis by US Environmental Protection Agency (EPA) Method 600, and US Department of Agriculture (USDA) Handbook 60 Method Number 24, were shipped to SVL Analytical, in Kellogg, Idaho. Samples for permeability testing were shipped to Daniel B. Stephens and Associates, in Albuquerque, New Mexico. A falling head method, as described in Klute and Dirksen, 1986, was used to determine the saturated hydraulic conductivity due to the low permeability of the materials. Samples for permeability testing were re-compacted by the laboratory to the approximate measured field density (or as close as possible) prior to conducting the tests.

Samples for paste pH were analyzed by HGC personnel in Tucson based on the method presented in Chapter 12.2.6 of McLean, 1982. Approximately 10 grams of air-dried soil was weighed in a Dixie® cup and approximately 20 grams of distilled water was added to the cup to obtain a 2:1 water to soil ratio. The samples were thoroughly mixed, allowed to stand for 10 minutes and then the paste pH was measured using a pH meter. The pH meter was calibrated and checked every 6 samples using a pH 7 and pH 10 buffer solution. The pH measurements were made at room temperature.

5. RESULTS

The results of the field testing and laboratory analysis of samples are provided in the sections below.

5.1 Ring Infiltrometer Tests

Water usage data collected during the performance of the ring infiltrometer tests are provided in Table 1. Water level data collected during performance of the evaporation tests are provided in Table 2. Table 1 also contains the calculated net water usage rates for the two tests, and Table 2 the calculated evaporation rate used to compute the net infiltration rates in Table 1.

As shown in Tables 1 and 2, the average net water usage rate (total usage - evaporation) was somewhat higher during the initial portion of both tests than during the latter portion of the tests, which is typical behavior until "steady-state" conditions are reached. The overnight data from both tests were assumed to represent stable conditions and were considered more representative because conditions were less windy and evaporation rates lower. It is likely, however, that lower net water usage rates would have resulted if the tests were conducted for a longer period of time because "steady-state" conditions may not have been achieved during the test duration. Furthermore, as discussed in Section 4.3, the observed leakage from around the outer edge of the ring infiltrometer during the tests, and the unavoidable disturbance to the ore pad surface resulting from installation

of the ring into the hard, compacted surface of the ore pad, resulted in higher water usage rates than would have occurred had these conditions not been present. The water usage rates are therefore considered unrepresentatively high.

A numerical model was used to calculate vertical permeability values for each location based on the measured overnight net water usage rates. A numerical model is needed primarily to account for lateral subsurface spreading of the infiltrating water. Water movement in the subsurface will not be entirely vertical due to the use of a single-ring infiltrometer for the tests. The numerical model will also account for the hydraulic head created by the height of water in the ring. TRACRN, a 3-dimensional, finite-difference flow and transport computer program capable of simulating flow and solute transport in variably saturated porous media, was used for the interpretation. TRACRN was developed at Los Alamos National Laboratories (Travis and Birdsell, 1988).

A 2-dimensional, radially-symmetric flow domain was simulated that included 20 cells (or nodes) extending to a total radial distance of approximately 28 feet in the radial direction, and 25 layers extending to a total depth of approximately 75 feet. Cell spacing was dense in the portion of the model representing the ring, as was the layer spacing near the surface, to reduce numerical error. The upper boundary of the model represented the site surface. Side and base model boundaries were located sufficiently far from the cells representing the ring to minimize boundary effects. The hydraulic head specified in the cells representing the ring was approximately equal to the water levels (height of water in ring above ore pad surface) maintained in the ring. Details of the

simulation, including the model construction and selection of parameters, and the mathematical basis for the code are provided in Appendix A.

Simulations for both infiltrometer tests were run until a steady water usage rate was obtained. The permeabilities of the soils represented in the model were adjusted until the steady water usage rate was approximately equal to the measured overnight net water usage rate for each test. Two simulations were run for each test, one assuming isotropic materials and the other assuming materials with a horizontal permeability equal to 10 times the vertical permeability. Results are summarized in Table 3. Vertical permeability estimates at test location #1 (16-15) were 1.2×10^{-5} centimeters per second (cm/s) and 6.3×10^{-6} cm/s for the isotropic and anisotropic cases, respectively, and at test location #2 (8-10), vertical permeability estimates were 5.2×10^{-6} cm/s and 2.6×10^{-6} cm/s for the isotropic and anisotropic cases, respectively. Vertical permeability estimates for the anisotropic cases are smaller because lateral subsurface spreading accounts for a larger proportion of the water usage.

Due to the observed leakage around the outer edge of the ring infiltrometer during the tests, however, and due to unavoidable disturbance to the surface resulting from installing the ring in the hard, highly-compacted, ore pad surface, and the relatively short time duration of the tests, the water usage rates are considered unrepresentatively high. The permeabilities computed from the ring infiltrometer test data are therefore considered to overestimate the actual permeabilities.

5.2 Laboratory Analysis of Permeability

The results of the laboratory analyses of permeability are provided in Table 4. Saturated permeabilities range from 1.2×10^{-6} cm/s to 3.5×10^{-8} cm/s, with a geometric mean of 2×10^{-7} cm/s. The highest value is lower than the lowest value estimated from the ring infiltrometer tests, and the average is approximately an order of magnitude lower than the lowest permeability estimated from the ring infiltrometer tests, which is consistent with the conclusion that the permeabilities calculated from the ring test data are overestimates.

As discussed in Section 4.3 and Section 5.1, in conducting the ring infiltrometer tests, the difficulty in maintaining a seal around the ring, the unavoidable disturbance resulting from installation of the ring into the hard, highly compacted ore pad surface, and the relatively short time duration of the tests which made achievement of "steady-state" conditions unlikely, resulted in unrepresentatively high water usage rates, and therefore, overestimation of vertical permeability. Because these conditions could not be quantified or reliably taken into account in interpreting the ring infiltrometer data, the results of the laboratory analyses of permeability, although subject to all the uncertainties resulting from the unavoidably disturbed nature of the samples, are considered more reliable, and are more consistent with the measured, densely compacted nature of the ore pad surface (Sections 5.3 and 5.4).

5.3 Nuclear Density Tests

The results of nuclear density and moisture content tests using the nuclear gauge are provided in Table 5. Wet densities ranged from 113 to 145 pounds per cubic foot (lb/ft^3) and averaged $130 \text{ lb}/\text{ft}^3$. Dry densities ranged from 108 to $138 \text{ lb}/\text{ft}^3$ and averaged $123 \text{ lb}/\text{ft}^3$. Moisture content varied from 3.3 to 11.5 %. These results indicate a high degree of compaction with porosities averaging about 26%, assuming a grain density of $167 \text{ lb}/\text{ft}^3$ ($2.67 \text{ grams per centimeter cubed [g}/\text{cm}^3]$) (Hillel, 1980). The dry densities measured at the locations of the ring infiltrometer tests, 16-15 (Test #1) and 8-10 (Test #2), are $127 \text{ lb}/\text{ft}^3$, and $132 \text{ lb}/\text{ft}^3$, respectively. These values are within 4% of each other, and within 7% of the average value of $123 \text{ lb}/\text{ft}^3$ based on all the nuclear density tests. These data indicate that the compaction of the ore pad surface is relatively uniform.

5.4 Sand Cone Density Tests

The results of the sand cone density tests are provided in Table 6. Wet densities ranged from 118.5 to $137 \text{ lb}/\text{ft}^3$, averaging $127 \text{ lb}/\text{ft}^3$, and are similar to those obtained by the nuclear gauge tests.

Differences in wet densities calculated by the two methods were less than 1% at locations 7-4 and 8-10, less than 5% at locations 18-19A and 16-15, and less than 11% at location 17-4. These differences are not considered significant.

5.5 Laboratory Analysis of Grain Size Distribution, Moisture Content, Organic Carbon Content, Neutralization Capacity, and Paste pH

The results of laboratory analysis of grain-size distribution, moisture content, total organic carbon, neutralization capacity, and paste pH are summarized in Tables 7 through 10. Laboratory analytical reports are provided in Appendix B. Sampled materials, as shown in Table 7, generally have a higher content of fines (silts and clays) than sands. Only two samples, at location 7-4, had sand content greater than 50%. Clay content ranged from approximately 15% to 28%, silt content from approximately 18% to 44%, and sand content from approximately 29% to 62%. The materials range from SM to ML in the United Soils Classification System (USCS) and can be generally described as loams (loams, clay loams, sandy clay loams, and sandy loams, as shown in Table 7). Total porosities for uncompacted materials of this type generally exceed 40% due to their fine-grained nature. The calculated average porosity of approximately 26% based on the nuclear density tests indicates that the materials have undergone a high degree of compaction at the site. The composition of the ore pad materials, and the relatively uniform compaction of the materials (based on the nuclear density tests) are consistent with generally low permeabilities for the ore pad.

The paste pH measurements (Table 8) ranged from 7.4 to 8.3, indicating neutral to alkaline conditions. This is consistent with the neutralization capacity measurements shown in Table 9, which ranged from 11 tons calcium carbonate (CaCO_3)/1,000 tons (or approximately 1.1% CaCO_3 by weight) to approximately 141 tons CaCO_3 /1,000 tons (or approximately 14% CaCO_3 by weight) for samples collected at the site. Although mineral species other than calcium carbonate may

contribute to the measured neutralization capacities, these high values are consistent with the reported incorporation of crushed limestone into the ore pad during construction.

Total organic carbon content (Table 9) ranged from 0.17% to 0.68%, and are within a range generally typical for shallow desert soils. Moisture content (Table 10) varied from 2.3% to 12.4% and averaged 7.7% in samples submitted for analysis. At the two locations where both shallow (surface) and deeper samples were collected, the deeper materials had a higher measured moisture content than shallow samples. The average moisture content determined from the nuclear density tests (5.6%) is somewhat lower than the average for the soil samples analyzed in the laboratory, which is reasonable considering that the nuclear density tests are more representative of shallower (surficial) materials, and that most (6 out of 9) samples submitted for laboratory moisture analysis were collected at depths of approximately 2 feet.

6. EVALUATION OF POTENTIAL SEEPAGE FROM FEED STOCKPILES ORIGINATING AS PRECIPITATION

The potential for precipitation to infiltrate feed stockpiles temporarily stored on the ore pad and result in seepage from the base of a pile into the ore pad surface was evaluated using HELP3. HELP3 is a computer program that uses daily precipitation, solar radiation, and temperature data to evaluate the potential for infiltration of precipitation into cover soils at landfills, mines, and other facilities. A complete description of HELP3 is available in Schroeder et al. (1994).

For these simulations, a single layer of TYPE 1, representing a "vertical percolation layer" as defined in Schroeder et al (1994), was assigned material characteristics typical of feeds currently stored and anticipated to be stored on the ore pad. Two types of materials were simulated: 1) a predominantly fine-grained material corresponding to default material type 12 (USCS symbol CL, clay) that is generally representative of material currently stored on the site, and 2) a coarser-grained material corresponding to default material type 5 (USCS symbol SM, silty sand) that is representative of materials that may be stored in the future. The Maywood material anticipated to be stored on the site generally lies between these two material types but is more similar to default material type 5. Material type 12 has a permeability of 4×10^{-5} cm/s and material type 5 a permeability of 1×10^{-3} cm/s, which is conservatively high, and is nearly two orders of magnitude higher than that for type 12. The thickness of the materials comprising the simulated layer was assumed to be 15 feet, which is about the average thickness of feed piles currently on site, and the area of the layer 1 acre.

Weather data used were the 5 years of default data supplied by HELP3 for Cedar City, Utah. This is considered appropriate for purposes of this evaluation because Cedar City has a similar climate and precipitation and has approximately the same latitude and elevation as the White Mesa Site.

The evaporative zone depth, which indicates the maximum depth in the material that moisture can be made available for evaporative loss via upward movement by capillary action, is affected by factors that include the material type and climate. In general, the drier and sunnier the climate, and the finer-grained the material, the greater the evaporative zone depth. To be conservative, a depth of 18 inches was chosen for both material types, which is the minimum value suggested in the HELP3 manual for southern Utah. In the relatively thick (15-foot) zone that was simulated, therefore, only moisture in the upper 10% of the zone was modeled as available for evaporative loss.

HELP3 uses the Soil Conservation Service (SCS) curve number approach to compute the ratio of runoff to infiltration during a precipitation event. In each simulation, HELP3 was allowed to compute the curve number based on an average slope of 20%, a slope length of 100 feet, and assuming bare ground (no vegetation). The chosen slope and slope length values are considered conservative with respect to the geometries of the feed stockpiles currently on site, which have slopes as high as 45%, and slope lengths generally less than 100 feet. HELP3 computed an SCS curve number of 95.5 for material type 12 and 85.5 for material type 5. In general, the lower the

permeability of the material, the steeper the slope, and the longer the slope length, the higher the ratio of runoff to infiltration, and the higher the SCS curve number. Material type 5 has a lower SCS curve number because it has a higher permeability and consequently a higher potential for precipitation to infiltrate rather than run off.

Finally, HELP3 was allowed to assign initial moisture content equal to the "field capacities" of the materials, which is a conservatively high moisture content considering that most feeds would be expected to have lower initial moisture content as a result of excavation and transport to the White Mesa Site. Specification of this initially high moisture content will tend to result in overestimation of seepage through the layer, which provides for a conservative analysis.

The results of the simulations are shown in Table 11 for the two material types. Output for the two runs are provided in Appendix C. Average annual seepage is computed to be 0.0041 inches per year (in/yr) from material type 12, and 0.014 in/yr from material type 5. Because of the choice of conservative parameters for these simulations, as discussed above, these results most likely overestimate the actual seepage rates that may be expected at the site.

7. POTENTIAL FOR INFILTRATION OF SEEPAGE FROM FEED STOCKPILES INTO THE ORE STORAGE PAD

The potential seepage rate from feed stockpiles originating as precipitation is low based on the conservative analysis discussed in Section 6. The average annual seepage rate of 0.014 inches/year estimated for a relatively coarse-grained material stored on the site would penetrate, on average, approximately 0.021 feet into the ore pad in the 2 years that a feed typically would be stored on the site assuming an average porosity of 26% (as calculated in Section 5.3) and an average saturation of 42% in this depth interval. The saturation of 42% is based on the average moisture content of 5.6% by weight, the 26% porosity, and the average dry bulk density of 123 lb/ft³ (1.97 g/cm³) determined from the nuclear gauge density measurements:

This calculation assumes that the ore pad has a high enough average permeability (10^{-6} to 10^{-7} cm/s) to accept this small amount of seepage (0.014 in/yr = 1.1×10^{-9} cm/s) without a significant change in water saturation, and that the seepage will move downward, under unsaturated flow conditions, at the same rate as the incoming seepage. In moving downward, the seepage is assumed to displace existing pore waters, but to move through approximately the same average cross-sectional area occupied by the existing pore waters.

The average depth of penetration is therefore calculated as:

$$d = \frac{i}{\theta} \cdot t$$

where:

d = average depth of penetration (feet)

i = seepage rate in cubic feet per square foot per year $\left(\frac{\text{ft}^3}{\text{yr}\cdot\text{ft}^2} \right) = \text{feet/year (ft/yr)}$

θ = volumetric water content (equal to the product of porosity and saturation), and

t = time (years)

Although some seepage is estimated to occur during temporary storage, once the feed materials were removed from the ore pad, the surface would be subject to evaporative losses, and most of any seepage that had potentially infiltrated the pad to the shallow calculated depth of 0.021 feet would be likely to evaporate. This evaporative loss is supported by laboratory moisture content measurements at sample locations 7-4 and 8-10 where samples were collected at the surface and at approximately 2 feet bls (Table 10). The surface samples averaged 4.7% moisture and the deeper samples averaged 9.6% moisture, indicating an upward gradient consistent with evaporative loss from the surface of the ore pad.

Even if no evaporative losses occurred, assuming a continuous seepage rate of 0.014 in/yr (1.2×10^{-3} ft/yr), the average porosity of 26% and average water saturation of 42%, over an assumed site operational life of 50 years, seepage would only penetrate an average of approximately ½ foot below the ore pad surface, which is within the evaporative zone depth. This is a conservative calculation because it assumes a continuous source over the 50-year operational period, when in fact the source would be discontinuous during site operation. Furthermore, during periods when the

sources were not present, the ore pad surface would be subject to evaporative losses, further reducing the long-term penetration depth.

8. POTENTIAL FOR TRANSPORT OF CONSTITUENTS PRESENT IN FEED STOCKPILES INTO THE SUBSURFACE

The potential for transport of a constituent originating from the feed stockpiles temporarily stored on the site into the subsurface depends on factors that include the seepage rate and the type of constituent (for example, a metal or organic compound), the concentration, the solubility, the volatility, and the potential for retardation and chemical or biological breakdown of the constituent. To the extent that these constituents exist in a mobile form (dissolved in pore waters or in the pore gases, or existing as a low viscosity separate liquid phase), they have the potential to be transported into the subsurface where they may migrate into deeper zones and potentially impact perched water at the site.

The potential for transport of constituents that are mobile primarily in the dissolved (aqueous) phase is low based on the analysis provided in Section 7. Examples of such constituents include metals, low volatility organic compounds (such as semi volatile organic compounds [SVOCs]), and volatile organic compounds (VOCs) that have relatively high solubilities. The mobility of SVOCs will be further limited by their generally low solubilities because only a small fraction of the mass of the SVOCs at any given time can exist in the mobile dissolved phase. Low solubility VOCs, which exist to a large degree in the vapor phase, may additionally be transported via vapor-phase diffusion.

8.1 Constituents Potentially Present in Feed Stockpiles

Compounds that may potentially be present in feed stockpiles include metals such as lead, SVOC's such as phthalates and polynuclear aromatic hydrocarbons (PAHs), and VOCs such as trichloroethene (TCE), chloroform, and BTEX (benzene, toluene, ethylbenzene, and xylenes). Prior to excavation and transport to the site, concentrations of VOCs and SVOCs in materials currently and anticipated to be stored on site (such as the Maywood materials) are reported to be in the parts per billion (ppb) range and low parts per million (ppm) range, respectively. The relatively low concentrations of VOCs reported in the feed materials are not indicative of a separate liquid phase. IUSA reports that SVOC concentrations in materials currently on site (Ashland) are within the low ppm (<10 ppm) range, that chlorinated VOCs are not detected, and that BTEX are either not detected or are detected only in the ppb range. Metals concentrations are reported to be as high as approximately 1,000 ppm, however, IUSA reports that post-excavation samples of the materials collected by International Technology Corporation (IT) passed Toxicity Characteristic Leaching Procedure (TCLP) tests for all metals.

8.2 Discussion of Behavior of Relatively Conservative Constituents

Constituents that behave relatively conservatively include dissolved constituents that experience little or negligible retardation or breakdown in the subsurface and that are transported entirely or at least predominantly in the dissolved phase. Some metals, some SVOCs, and some highly soluble VOCs can behave relatively conservatively. Conservative solutes will tend to move

at about the average velocity of any seepage potentially passing from the stockpiled feeds into the ore pad. Due to dispersion, a portion of the solute mass may, however, travel faster than the average seepage velocity. Based on the analysis provided in Section 7, however, the potential for transport of relatively conservative constituents is very low because the potential for generating seepage is low. The worst case estimate for seepage originating from a stockpile of relatively coarse-grained material, as discussed in Section 7, was 0.014 in/yr (0.0012 ft/yr). Assuming continuous seepage at this rate, which is very conservative considering that the potential sources would be discontinuous, and assuming a site operational life of 50 years, seepage would only move about ½ foot into the subsurface, on average, based on the assumptions presented in Section 7. This would also be the approximate transport depth for a conservative constituent if dispersion is assumed to be negligible.

8.3 Retardation of Constituents in the Subsurface

SVOCs and VOCs potentially present in the feed stockpiles at the site are likely, however, to experience significant retardation in the subsurface, and would be expected to move significantly more slowly than the average seepage velocity, and could migrate less than about ½ foot into the subsurface over the assumed 50-year operational lifetime. Chloroform, for example, would have a retardation factor of 2.52 and a relative velocity of 0.43 based on a bulk density of 2 g/cm³, the measured average fraction of organic carbon (f_{oc}) of 0.0033 in the ore pad, and a K_{oc} of 53 milliliters per gram (mL/g), meaning it would move on average at only 43% of the average seepage velocity. A phthalate such as butyl benzyl phthalate would have a retardation factor of 345 and a relative velocity of 2.9×10^{-3} based on its K_{oc} of 13,746 mL/g, meaning it would move on average only at

0.29% of the seepage velocity. These calculations are based on the retardation equation provided in Freeze and Cherry (1979), and K_{oc} values reported in EPA (1996). Furthermore, chloroform and other organic compounds would experience some degree of chemical and/or biological breakdown over the 50-year period, further limiting their potential for downward transport.

Metals likely to exist in the feed stockpiles could only be transported into the subsurface dissolved in seepage, and most would experience some degree of retardation in the subsurface. Lead, for example, which is only mobile dissolved in acidic solutions, would precipitate out of solution upon entering the subsurface due to the high measured neutralization capacity of the ore pad. The potential for transport of metals that are mobile only under acidic conditions is negligible as long as sufficient neutralization capacity exists. It is highly unlikely that the high measured neutralization capacities at the site would be significantly diminished over the operational lifetime.

8.4 Vapor-Phase Transport

VOCs such as TCE and tetrachloroethylene (PCE) will have a significant portion of their total mass in the vapor phase. Concentrations of these compounds are likely to be substantially reduced through volatilization during excavation and transport of materials to the site, and during storage on the ore pad, and therefore have a very low potential for significant transport into the subsurface due to their likely low source concentrations once on site. Non-detect to low concentrations of BTEX compounds in materials currently stockpiled on site are reported to have been verified by sampling and analysis of these materials by IUSA. Furthermore, should these

compounds be transported from a feed stockpile into the shallow subsurface during temporary storage, they will be subject to volatilization from the shallow subsurface once the stockpiled materials are removed.

The combination of low source concentration, the discontinuous nature of the potential sources, and potential for post-source removal loss from the subsurface via volatilization make the potential for transport of VOCs into the subsurface very low. In addition, VOCs are subject to chemical and biological breakdown, further reducing their potential for significant downward transport.

8.5 Summary

In summary, the potential for transport of constituents likely to be present in feed stockpiles temporarily stored on the site to depths that may impact perched groundwater (currently about 65 feet below the ore pad surface) is almost negligible. Even conservative constituents dissolved in potential seepage (experiencing no retardation or chemical breakdown) would likely penetrate on average less than ½ foot into the subsurface, provided a source was continually active during an assumed 50-year site operation time, and assuming the conditions presented in Section 7.

The actual depth of penetration of most constituents likely to be present would be even less than ½ foot on average because:

- 1) seepage estimates are likely overestimated,
- 2) individual sources would actually be discontinuous, as feed stockpiles are stored at most for a 2-year period,
- 3) upon source removal, most of the seepage that had penetrated (as well as VOCs) would be likely to evaporate (and volatilize),
- 4) most constituents dissolved in seepage would be retarded in their downward movement relative to the seepage rate, and
- 5) most organic constituents would experience significant chemical and/or biological breakdown over a 50-year period.

Because the Nuclear Regulatory Commission (NRC)-approved Site Reclamation Plan for the site assumes costs for removal of 18 inches of soil from the Mill and ore pad area, any constituents that did infiltrate the upper ½ foot of the ore pad would be removed during site remediation. Thus, the long-term potential impact to perched groundwater can also be considered negligible.

9. CONCLUSIONS

An evaluation of the potential for seepage of constituents present in alternate feed materials temporarily stored on the ore storage pad into the subsurface indicates that the potential is low, and that even conservative constituents dissolved in the seepage, under worst case assumptions, are likely to penetrate on average only about ½ foot into the subsurface over an assumed 50-year site operational lifetime. This estimate assumes that sources are continuous over the 50-year period, that seepage originates as precipitation infiltrating the alternate feed stockpiles, and that no retardation or breakdown of these constituents occurs. The actual penetration of constituents, which could include metals, SVOCs, and VOCs, would likely be even less because:

- 1) the seepage rates are likely overestimated,
- 2) individual sources would actually be discontinuous, as feed stockpiles are stored at most for a 2-year period,
- 3) upon source removal, most of the seepage that had penetrated (as well as VOCs) would be likely to evaporate (and volatilize),
- 4) most constituents likely to be dissolved in seepage would be retarded in their downward movement relative to the seepage rate, and
- 5) most organic constituents would experience significant chemical and/or biological breakdown over a 50-year period.

In general, the low potential for seepage and transport is due to the following:

- 1) the dry climate,
- 2) the low permeability, highly compacted nature of the ore pad surface,

- 3) the high neutralization capacity of the materials underlying the ore storage pad that would immobilize acid-soluble metals,
- 4) the presence of organic carbon in the materials underlying the ore pad that would retard the movement of organic compounds, and
- 5) the generally low concentrations of mobile organic compounds in the feed materials.

As a result of the low potential for generation of seepage and transport of constituents, and considering that the site is likely to operate for a time period on the order of only tens of years, the potential for impact to perched groundwater is considered negligible. Furthermore, because the NRC-approved Site Reclamation Plan assumes costs for removal of 18 inches of soil from the Mill and ore pad areas, any constituents that did infiltrate the upper ½ foot of the ore pad would be removed during site reclamation. Thus, the long term potential for impact to perched groundwater can also be considered negligible.

10. REFERENCES

- Freeze, R.A. and J.A. Cherry. 1979. *Groundwater*. Prentice-Hall, Inc., Englewood Cliffs, N.J.
- Hillel, 1980. *Fundamentals of Soil Physics*. Academic Press.
- Hydro Geo Chem, Inc. 2001. *Assessment of the Effectiveness of Using Existing Monitoring Wells for GWDP Detection Monitoring at the White Mesa Uranium Mill, Blanding, Utah*. Submitted to International Uranium (USA) Corporation.
- Klute, A. and C. Dirksen. 1986. *Hydraulic Conductivity and Diffusivity: Laboratory Methods in Methods of Soil Analysis, No. 9:1*. A. Klute et al. eds. American Society of Agronomy, Inc. and Soil Science Society of America, Inc., Madison, Wisconsin. Pp. 687-734.
- McLean, E.O. 1982. *Soil pH and Lime Requirement in Methods of Soil Analysis, No. 9:2*. A.L. Page et al. eds. American Society of Agronomy, Inc. and Soil Sciences Society of America, Inc., Madison, Wisconsin. Pp. 199-224.
- Schroeder, P.R., N.M. Aziz, C.M. Lloyd, and P.A. Zappi. 1994. *The Hydrologic Evaluation of Landfill Performance (HELP) Model: User's Guide for Version 3*. EPA/600/R-94/168a. U.S. Environmental Protection Agency Office of Research and Development, Washington D.C. September 1994.
- Titan. 1994. *Hydrogeologic Evaluation of the White Mesa Uranium Mill*. Submitted to Energy Fuels Nuclear.
- Travis B.J. and K.H. Birdsell. 1988. *TRACRN 1.0. A Model of Flow and Transport in Porous Media for the Yucca Mountain Project - Model Description and Users Manual*. Submitted to Yucca Mountain Project Milestone T421.
- United States Environmental Protection Agency. 1996. *Soil Screening Guidance, Second Edition*. Office of Solid Waste and Emergency Response, Washington D.C. Publication 9355.4-23. July 1996.

TABLES

TABLE 1
Ring Infiltrometer Test Data

Test #1

Date	Time	Change in Volume (gal)	Change in Volume (ft ³)	Change in Time (days)	Rate (ft/day)	Evaporation Rate (ft/day)	Water Usage Net Rate (ft/day)	Comment
5/20/2002	11:12	0	--	--	--	--	--	start
	15:36	3	0.4	0.18	0.22	0.088	0.13	
	15:45	0	--	--	--	--	--	tank refilled
	20:30	3.55	0.48	0.20	0.24	0.049	0.19	
	20:37	0	--	--	--	--	--	tank refilled
5/21/2002	7:07	4	0.53	0.44	0.12	0.020	0.10	

Test #2

Date	Time	Change in Volume (gal)	Change in Volume (ft ³)	Change in Time (days)	Rate (ft/day)	Evaporation Rate (ft/day)	Water Usage Net Rate (ft/day)	Comment
5/21/2002	9:58	0	--	--	--	--	--	start
	11:30	1.25	0.17	0.06	0.27	0.115	0.16	
	15:54	3.25	0.27	0.19	0.14	0.115	0.03	
	16:00	--	--	--	--	--	--	tank refilled
	17:12	0.25	--	--	--	--	--	
5/22/2002	7:40	3.15	0.39	0.60	0.06	0.020	0.040	

Note: Area of ring is approximately 10 ft²

TABLE 2**Evaporation Test Data**

Date	Time	Gauge Water Level (inches)	Change in Water Level (inches)	Change in Water Level (feet)	Change in Time (days)	Evaporation Rate (feet/day)
5/20/2002	13:30	3.768	--	--	--	--
	15:27	3.680	0.088	0.0073	0.083	0.088
	20:30	3.559	0.121	0.0101	0.208	0.049
5/21/2002	7:07	3.446	0.113	0.0094	0.442	0.021
	11:30	3.238	0.208	0.0173	0.151	0.115
	16:15	2.964	0.274	0.0228	0.198	0.115
5/22/2002	8:45	2.800	0.164	0.0137	0.688	0.020

TABLE 3
Vertical Permeability Estimates Based on the Results of Ring Infiltrometer Tests and Numerical Modeling

	Test # 1	Test # 2
Permeability (cm/s) for ¹ isotropic case	1.2×10^{-5}	5.2×10^{-6}
Permeability (cm/s) for ² anisotropic case	6.3×10^{-6}	2.6×10^{-6}

Notes:

- ¹ isotropic case: *horizontal and vertical permeabilities are equal*
- ² anisotropic case: *horizontal permeability is 10 times the vertical permeability*

TABLE 4
Laboratory Analysis of Saturated Hydraulic Conductivity

Location	Sample Number	Saturated Permeability K_{sat} (cm/sec)	Method of Analysis
16-15	#1 @ surface	5.4E-07	Falling head
17-4	#3 @ surface	3.5E-08	Falling head
7-4	7-4 @ surface	1.2E-06	Falling head
8-10	8-10 @ surface	1.2E-07	Falling head
8-10	8-10 @ 2 feet	1.1E-07	Falling head

TABLE 5
Nuclear Field Density Test Results

Test Number	Location	Probe Depth (inches)	Wet Density (lb/ft ³)	Dry Density (lb/ft ³)	Moisture Content (weight %)	Soil Type
1	8-10	4.0	137.8	132.1	4.3	Clay, hard
2	8-9	4.0	132.2	126.5	4.6	Clay, hard
3	9-10	2.0	113.0	107.8	4.8	Clay, hard
4	9-11	4.0	130.9	125.7	4.2	Clay, hard
5	7-11	2.0	126.7	120.4	4.8	Clay, hard
6	8-14	4.0	117.1	110.5	6.0	Clay, hard
7	10-16	4.0	136.3	130.8	4.2	Clay, hard
8	11-17	4.0	128.8	122.4	5.2	Clay, hard
9	10-20	4.0	124.6	118.1	5.5	Clay, hard
10	10-22	4.0	134.6	130.2	3.4	Clay, hard
11	18-19	4.0	130.6	123.6	5.6	Clay, hard
12	17-18	4.0	130.4	124.3	4.9	Clay, hard
13	17-16	4.0	134.4	130.0	3.3	Clay, hard
14	16-15	4.0	133.8	127.3	5.1	Clay, hard
15	15-14	4.0	122.1	115.2	6.0	Clay, hard
16	13-14	4.0	125.7	115.6	8.7	Clay, hard
17	16-12	4.0	122.3	114.4	6.7	Clay, hard
18	16-13	4.0	126.0	119.0	5.9	Clay, hard
19	18-12	4.0	125.8	118.2	5.7	Clay, hard
20	16-11	4.0	144.7	138.4	4.6	Clay, hard
21	15-10	4.0	118.1	112.2	5.3	Clay, hard
22	13-9	4.0	125.8	120.3	4.5	Clay, hard
23	12-10	4.0	133.2	127.9	4.1	Clay, hard
24	11-11	4.0	122.2	114.8	6.5	Clay, hard
25	17-4	4.0	134.3	124.1	8.3	Clay, hard
26	18-7	4.0	134.0	127.4	5.2	Clay, hard
27	7-4	4.0	122.5	117.3	4.4	Clay, hard
28	9-6	4.0	137.3	128.0	7.2	Clay, hard
29	10-5	4.0	119.4	110.5	8.1	Clay, hard
30	10-4	4.0	119.6	111.9	6.9	Clay, hard
31	10-1	4.0	143.3	128.5	11.5	Clay, hard
32	8-3	4.0	132.7	127.2	4.4	Clay, hard
33	5-5	4.0	128.8	122.4	5.2	Clay, hard
34	15-22	4.0	135.6	129.0	5.1	Clay, hard
35	13-23	4.0	134.6	127.8	5.3	Clay, hard
36	11-23	4.0	140.6	135.8	3.6	Clay, hard
37	15-24	4.0	135.1	128.8	4.8	Clay, hard
38	16-25	4.0	136.2	124.3	9.6	Clay, hard
39	15-27	4.0	141.2	134.2	5.2	Clay, hard
Average			130.1	123.2	5.6	

TABLE 6
Sand Cone Density Tests

Wet Density Determination

Test Number	Weight of Sand Before Calibration (lb)	Weight of Sand After Calibration (lb)	Calibration Weight (lb)	Weight of Sand Used (lb)	Weight of Sand in Hole (lb)	Volume of Hole (ft³)	Weight of Wet Soil (lb)	Wet Density (lb/ft³)
18-19A	10.01	5.15	4.86	3.10	1.76	0.022	2.79	126.8
18-19B	11.67	7.36	4.31	3.31	1.06	0.013	1.54	118.5
16-15	11.09	6.48	4.61	3.45	1.16	0.015	2.02	134.7
7-4	12.67	7.32	5.35	3.21	2.14	0.027	3.30	122.2
17-4	12.51	8.01	4.50	3.33	1.17	0.015	1.82	121.3
8-10	11.51	6.50	5.01	3.18	1.83	0.023	3.15	137.0

Note:

Weight of calibrated sand 78.62 lb/ft³

TABLE 7
Grain Size Distribution

Location	Sample Number	Percent Gravel	Percent Sand	Percent Silt	Percent Clay	USCS Symbol	Description
16-15	#1 @ 0-6 inches	4.2	36.6	38.7	20.5	ML	loam
16-15	#1 @ 2 feet	0.6	28.9	43.6	26.9	ML	loam
18-19	#2 @ 0-6 inches	5.9	41.4	24.4	28.3	ML	sandy clay loam
18-19	#2 @ 2 feet	19.2	38.0	21.1	21.7	SM	sandy clay loam
17-4	#3 @ 0-4 inches	0.0	40.5	31.2	28.3	ML	clay loam
17-4	#3 @ 2 feet	0.2	44.0	33.3	22.5	ML	loam
7-4	# 7-4 @ surface	6.3	59.5	18.4	15.8	SM	sandy loam
7-4	# 7-4 @ 2 feet	1.6	61.6	21.5	15.3	SM	sandy loam
8-10	# 8-10 @ surface	15.5	44.1	23.7	16.7	SM	sandy loam
8-10	# 8-10 @ 2 feet	0.4	41.6	34.9	23.1	ML	loam

Note:

* Description based on Figure 4.3 in Hillel, 1980. *Fundamentals of Soil Physics*. Academic Press.

TABLE 8**Soil Paste pH Measurements**

Sample	Depth	First Run pH	Second Run pH	Soil (g)	Water (mL)	Water to Soil Ratio
8-10	2 feet	7.86	8.09	13.5	27	2:1
7-4	surface	7.72	7.89	12	24	2:1
7-4	2 feet	8.1	8.14	11	22	2:1
8-10	0-2 inches	7.48	7.62	12	24	2:1
8-10	surface	7.4	7.53	11	22	2:1
18-19	2 feet	8.23	8	10	20	2:1
17-4	surface	7.9	7.95	10	20	2:1
16-15	2 feet	8.32	8.08	10	20	2:1
17-4	2 feet	8.29	8.09	12	24	2:1
16-15	0-8 inches	8.05	7.96	10	20	2:1
18-19	0-6 inches	7.86	7.81	10	20	2:1

Note:*NA=not applicable**pH meter calibrated and checked every 6 samples with pH 7 and 10 buffer solution*

TABLE 9**Neutralization Capacity and Total Organic Carbon**

Location	Sample Number	Neutralization Capacity (tons CaCO₃/1000 tons)	Total Organic Carbon (%)
16-15	# 1 @ 0-6 inches	41.8	0.17
16-15	# 1 @ 2 feet	61.2	0.23
18-19	# 2 @ 0-6 inches	68.8	0.40
18-19	# 2 @ 2 feet	65.0	0.34
17-4	# 3 @ 0-4 inches	10.5	0.18
17-4	#3 @ 2 feet	92.4	0.24
7-4	7-4 @ surface	124.0	0.49
7-4	7-4 @ 2 feet	29.3	0.24
8-10	8-10 @ surface	112.0	0.68
8-10	8-10 @ 2 feet	141.0	0.37

TABLE 10
Moisture Content

Location	Sample ID	Weight Percent Moisture
16-15	# 1 at 10 inches	8.6
16-15	# 1 at 2 feet	10.0
18-19	# 2 at 2 feet	8.4
17-4	# 3 at 2 feet	11.5
7-4	7-4 at surface	4.3
7-4	7-4 at 2 feet	6.8
8-10	8-10 at surface	5.1
8-10	8-10 at 0-2 inches	2.3
8-10	8-10 at 2 feet	12.4

TABLE 11**Results of HELP3 Simulations****Input Parameters**

	Material Type 12 (CL)	Material Type 5 (mL)
Thickness (ft)	15	15
Permeability (cm/s)*	4×10^{-5}	1×10^{-3}
Porosity (%)*	47	46
Initial water content (%) ("field capacity")*	34	13.3
Evaporation depth (ft)	1.5	1.5
SCS curve number*	95.6	85.4

Notes:

* = computed by HELP3

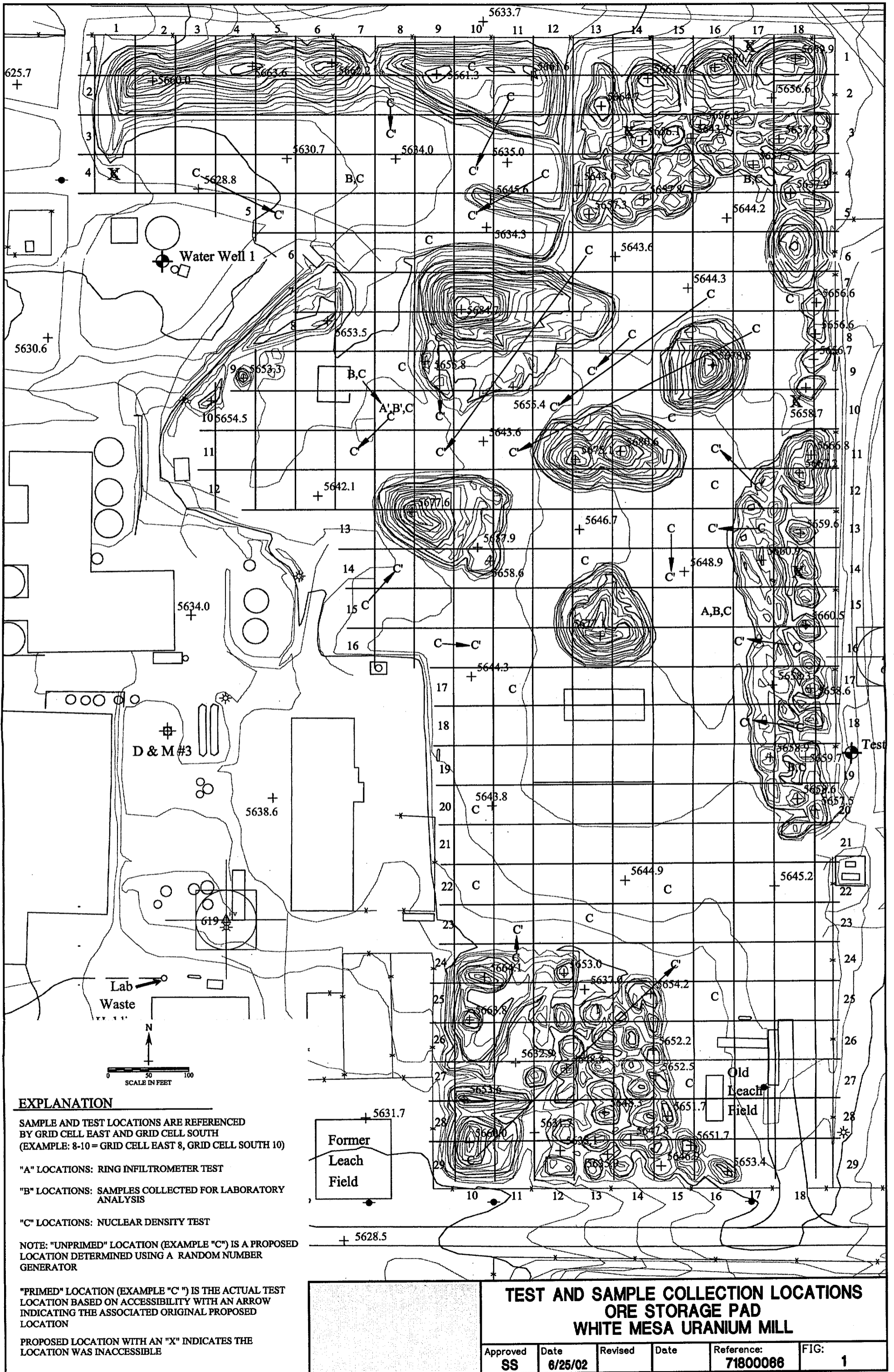
Seepage Estimates

	Material Type 12	Material Type 5
Average annual seepage rate (inches/year)	0.0041	0.014

Note:

see Appendix C for output details

FIGURES



EXPLANATION

SAMPLE AND TEST LOCATIONS ARE REFERENCED BY GRID CELL EAST AND GRID CELL SOUTH (EXAMPLE: 8-10 = GRID CELL EAST 8, GRID CELL SOUTH 10)

"A" LOCATIONS: RING INFILTRMETER TEST

"B" LOCATIONS: SAMPLES COLLECTED FOR LABORATORY ANALYSIS

"C" LOCATIONS: NUCLEAR DENSITY TEST

NOTE: "UNPRIMED" LOCATION (EXAMPLE "C") IS A PROPOSED LOCATION DETERMINED USING A RANDOM NUMBER GENERATOR

"PRIMED" LOCATION (EXAMPLE "C'") IS THE ACTUAL TEST LOCATION BASED ON ACCESSIBILITY WITH AN ARROW INDICATING THE ASSOCIATED ORIGINAL PROPOSED LOCATION

PROPOSED LOCATION WITH AN "X" INDICATES THE LOCATION WAS INACCESSIBLE

**TEST AND SAMPLE COLLECTION LOCATIONS
ORE STORAGE PAD
WHITE MESA URANIUM MILL**

Approved SS	Date 6/25/02	Revised	Date	Reference: 71800066	FIG: 1
----------------	-----------------	---------	------	------------------------	-----------

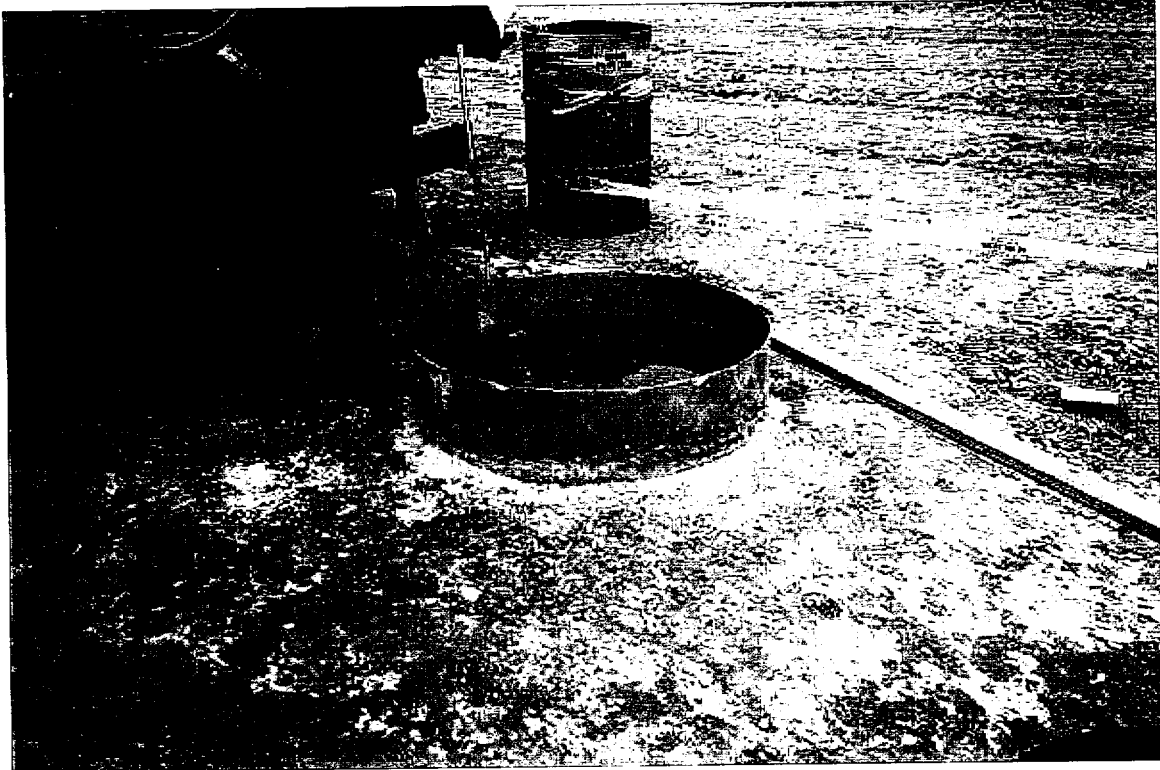


Figure 2. Ring infiltrometer test. Note seepage by geologist's foot.

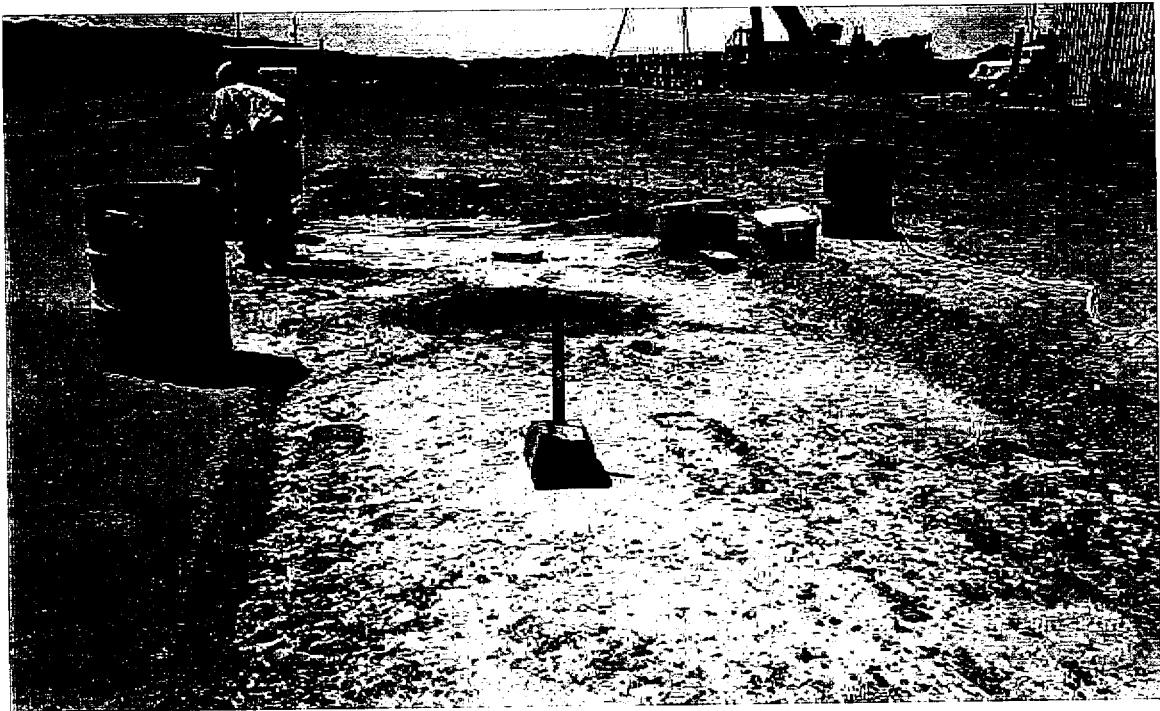


Figure 3. Nuclear density test performed near infiltrometer test location #1.



Figure 4. Nuclear density test performed at randomly selected sampling location.

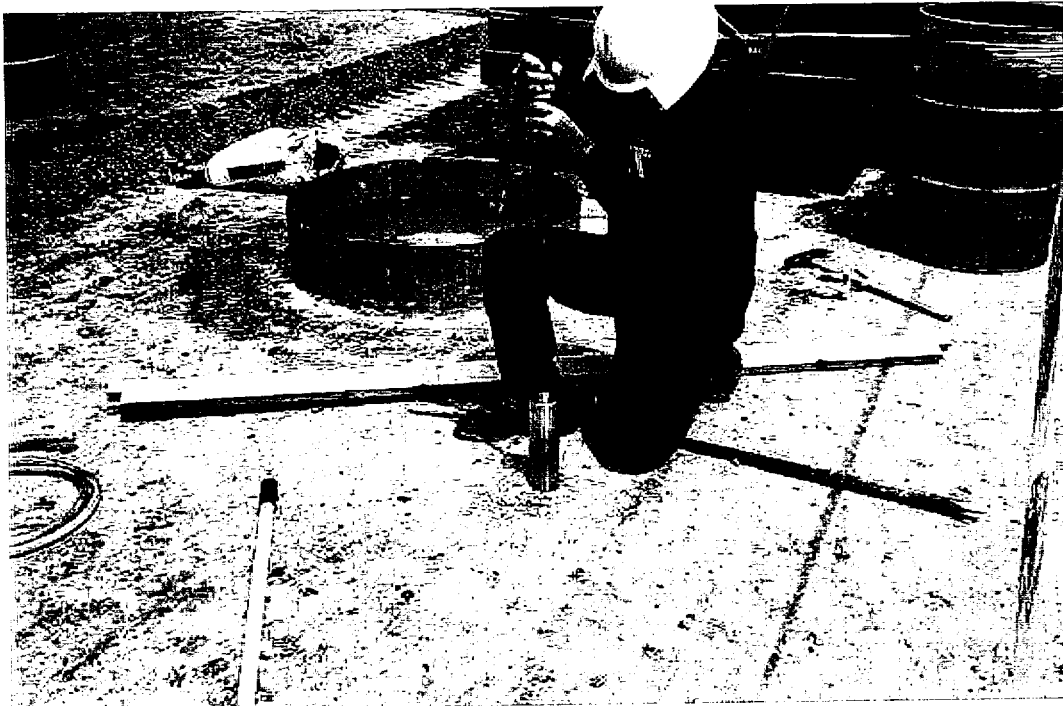


Figure 5. Attempt to collect undisturbed sample from compacted surface of ore pad using a ring barrel sampler.



Figure 6. Excavation used for sample collection. Note lighter horizon of ore pad surface and calcareous materials in darker subsurface along vertical face.



Figure 7. Typical sand cone test.

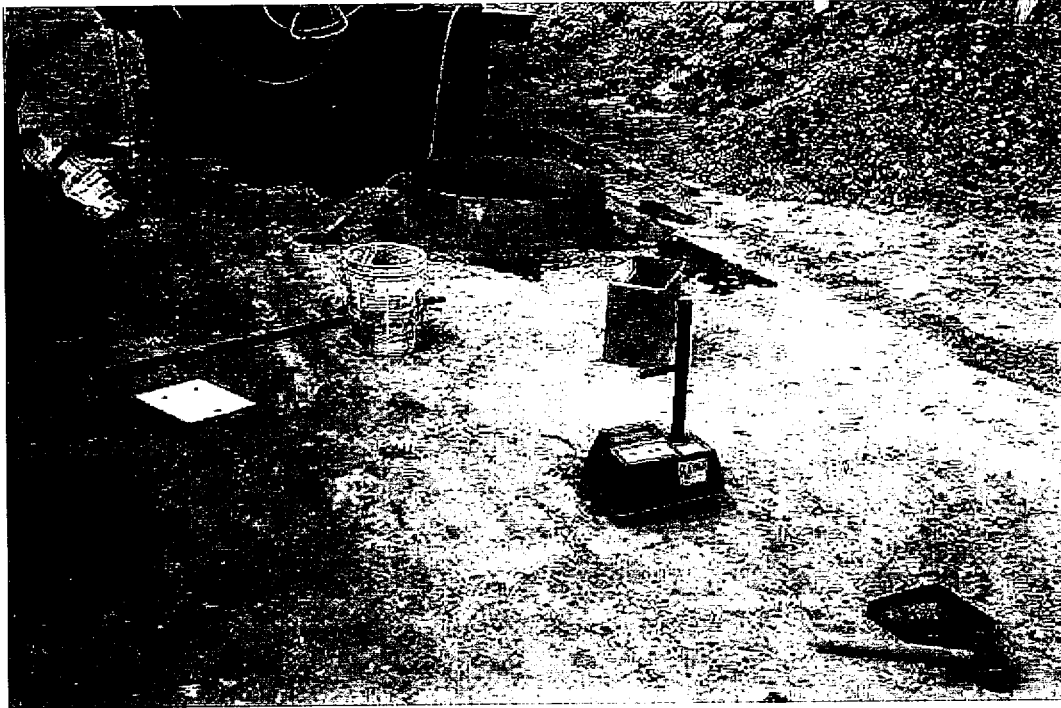


Figure 8. Infiltrometer location #2. Nuclear density gauge shown in foreground.

APPENDIX A

NUMERICAL MODELING OF RING INFILTRMETER TESTS

TABLE OF CONTENTS

A.1 Model Construction	1
A.2 Boundary Conditions	2
A.3 Model Parameters	3
A.4 Results	3
A.5 References	4

TABLE

- A.1 Parameters Specified in the Numerical Model

FIGURE

- A.1 Upper 30 Feet of the Numerical Model Mesh

ATTACHMENT

- A Description of TRACRN

APPENDIX A

NUMERICAL MODELING OF RING INFILTRATION TESTS

This appendix describes the methods and the numerical model used to estimate the vertical permeability of the ore storage pad based on data collected from the ring infiltrometer tests. The use of a numerical model is necessary to account for the lateral subsurface spreading of infiltrating water resulting from use of a single ring and for the hydraulic head created by the water level in the ring. Unless these factors are taken into consideration in the analysis, the vertical permeability will be overestimated. As described in the main text, two cases were simulated for each test. One assumed isotropic conditions (horizontal and vertical permeabilities are equal), and the other assumed an anisotropy factor of 10 (horizontal permeability = 10 times the vertical permeability). The greater the ratio of horizontal to vertical permeability, the more subsurface lateral spreading of infiltrating water will occur, and the lower the vertical permeability that will be estimated from the infiltration data. A horizontal to vertical permeability ratio of 10 is common for layered media and unconsolidated alluvial materials. The assumption of isotropic conditions is conservative, and will result in higher vertical permeability estimates.

A.1 Model Construction

The numerical model was constructed using TRACRN, a 3-dimensional, finite difference computer program developed at Los Alamos National Laboratories that is capable of simulating

liquid and gas flow, and solute transport, in variably saturated porous media. A complete description of the mathematical basis of TRACRN is provided in the attachment.

A 2-dimensional, radially symmetric flow domain was simulated using cylindrical coordinates. The simulated flow domain extended approximately 28 feet in the radial direction and to a total depth of 75 feet in the vertical direction. Twenty cells of variable spacing were specified in the radial direction and 25 layers of variable thickness were specified in the vertical direction. Figure A.1 is a 2-dimensional vertical cross section of the upper 30 feet of the model mesh that illustrates the cell spacing.

As shown in Figure A.1, the five cells along the upper boundary located closest to the left (interior) boundary were used to simulate the ring infiltrometer. In the uppermost layer of the model, all cells outside the ring were assigned a very low permeability (10^{-12} centimeters per second [cm/s]) to prevent lateral spreading in this layer. Therefore, no lateral spreading could occur within the upper inch of the model. Cell widths near the edge of the ring, as shown in Figure A.1, were smaller, and near surface layers more closely spaced to reduce the potential for numerical error.

A.2 Boundary Conditions

All model boundary cells were specified no flow except the upper boundary cells representing the ring, and all cells along the right-hand boundary. The right-hand boundary was maintained at initially specified pressures and saturations (“ambient” boundary condition).

Fully-saturated conditions and a water pressure approximately equal to the measured water level in the ring during the tests were maintained in the five upper boundary cells representing the ring. The left-hand boundary was coincident with the center of the ring (and the center of the model domain). The lowest layer of the model was maintained in a saturated condition to allow flow of water out the right-hand boundary, and prevent build-up of water at the base of the model.

A.3 Model Parameters

Parameters used in the model are provided in Table A.1. Unsaturated flow parameters such as bubbling pressure, irreducible liquid saturation, and pore size distribution index were based on values reported in Case et al., 1983, and Travis and Birdsell, 1988. Porosities and saturations specified in the model were the approximate average values determined from the nuclear density gauge tests.

A.4 Results

A simulation was run for each ring infiltrometer test for both isotropic and anisotropic cases. Simulations were run for a period of time sufficient to obtain a steady simulated infiltration rate. The permeabilities specified were then adjusted until the simulated steady infiltration rates were approximately equal to the field-measured net overnight infiltration rates. The results are shown in Table 3 of the main text.

A.5 References

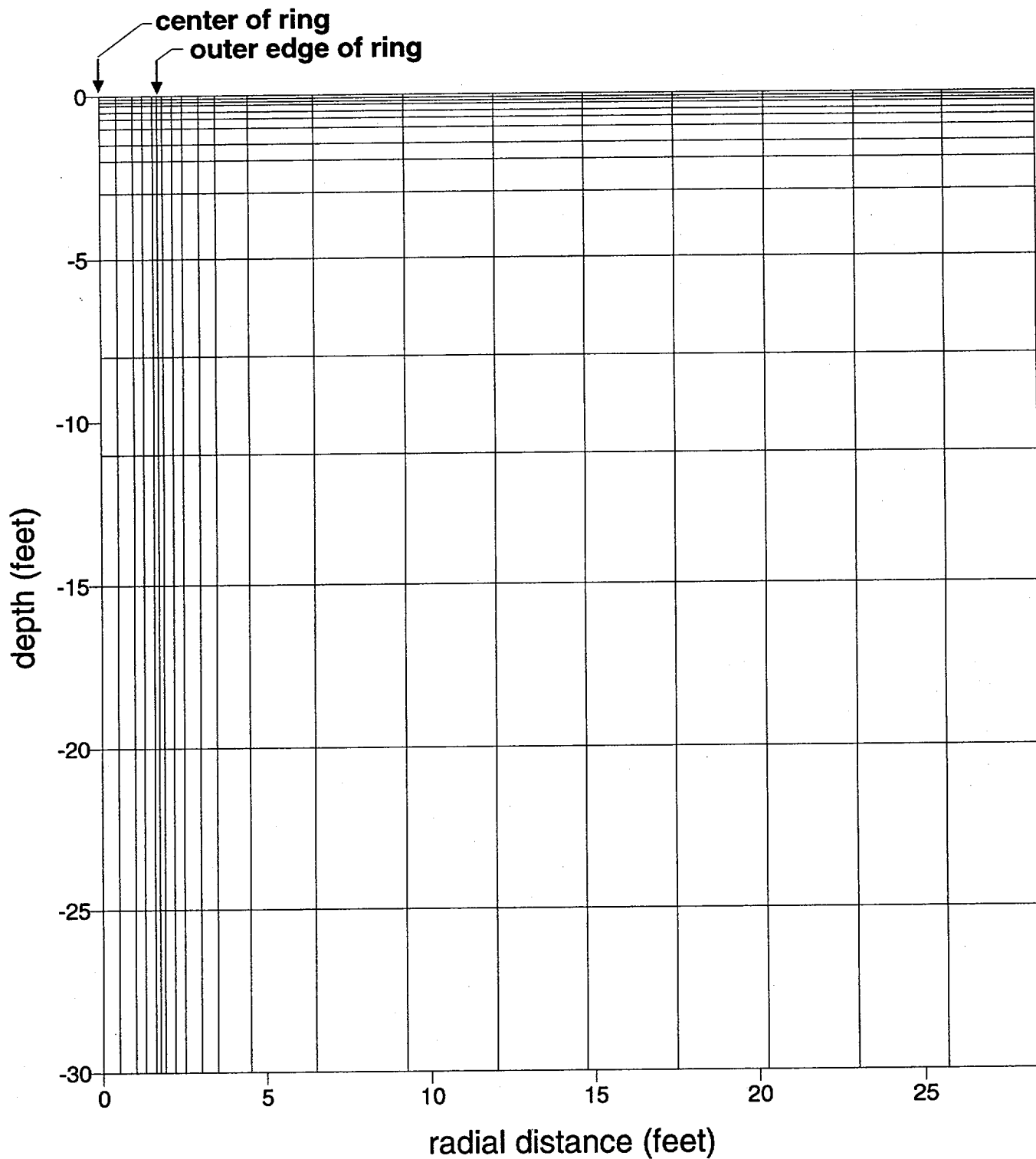
- Case, C., M. Kantsky, P. Kearl, R. Goldfarb, S. Leath, and L. Metcalf. Unsaturated Flow Properties Data Catalog, Volume I, Publication 45033. Water Resources Center, Desert Research Institute, University of Nevada System. October 1983.
- Travis B.J. and K.H. Birdsell. 1988. TRACRN 1.0. A Model of Flow and Transport in Porous Media for the Yucca Mountain Project - Model Description and Users Manual. Submitted to Yucca Mountain Project Milestone T421.

TABLE

TABLE A.1
Material Properties Used in the Numerical Model

Porosity	0.26
Bubbling Pressure (dyn/cm ²)	2.0x10 ⁴
Irreducible Water Saturation	0.40
Pore Size Distribution Index	2.6
Initial Water Saturation	0.42

FIGURE



**HYDRO
GEO
CHEM, INC.**

**UPPER 30 FEET OF NUMERICAL
MODEL GRID MESH**

APPROVED

DATE

REFERENCE

H:/718000/tracm/ringinfl/grid2ub.srf

FIGURE

A.1

ATTACHMENT A.1
DESCRIPTION OF TRACRN

ATTACHMENT A.1: DESCRIPTION OF TRACRN

This attachment contains a copy of portions of a report entitled, "TRACRN 1.0: A model of flow and transport for the Yucca Mountain Project-Model Description and Users Manual" by B.J. Travis and K.H. Birdsell, (Los Alamos National Laboratory TWS-ESS-5/10-88-08). Although TRACRN was developed specifically to solve problems of gas and water movement in support of the Yucca Mountain nuclear waste isolation project, it is a general purpose program suitable for application to a wide variety of environmental simulations involving gas and water movement.

The following pages describe the mathematical basis for the simulation air and water flow, and transport in both phases.

B. Mathematical Model

1. **Governing Equations.** The equations that comprise the TRACRN model are the mass and chemical species conservation equations, a reduced form of the momenta equations, and an equation of state plus several constitutive relations. The notation used throughout this report is given in Table I. Conservation of mass for the gas component is

$$\partial_t(\epsilon \rho_g \sigma_g) + \nabla \cdot (\rho_g \bar{u}_g) = \epsilon S_g \quad (1)$$

and for the liquid component is

$$\partial_t(\epsilon \sigma_l \rho_l) + \nabla \cdot (\rho_l \bar{u}_l) = \epsilon S_l \quad (2)$$

For isothermal systems in which water vapor is neglected, no diffusion or dispersion of water or air occurs. Equations (1) and (2) cover conditions of flow ranging from fully water saturated to fully air saturated.

The momenta conservation equations are solved in a reduced form known as Forchheimer's equations

$$\left[1 + \frac{1}{(1-\epsilon)} \frac{L \rho_i |\bar{u}_i|}{85.7 \mu_i} \right] \bar{u}_i = -\frac{k_i}{\mu_i} (\nabla P_i + \rho_i \hat{g}) \quad (3)$$

where the subscript i refers to a gas or liquid phase. This form neglects the acceleration term and uses a phenomenological treatment of inertial terms and viscous drag. At low Reynolds number (<10), this expression reduces to the well-known Darcy equation; at higher Reynolds number, the nonlinear term in Eq. (3) becomes important. Equation (3) gives excellent agreement (Dullien 1979) with steady, single phase flow data for Reynolds numbers up to about 100. Reynolds numbers much higher than a few hundred are rarely encountered in most flows through porous, permeable geomedial. We assume Eq. (3) is approximately valid for transient two-phase flow.

TABLE I. Notation Used In TRACRN

Parameter	Description	Units
A	cell interface area	(cm ²)
[A]	matrix containing the derivatives of the residuals with respect to P for the entire mesh	
[A _c]	matrix containing the derivatives of the residuals with respect to C for the entire mesh	
A _H	Constant relating the total amount of tracer in a volume to the liquid concentration	
{b}	generic residual vector	
{b _c }	vector of residuals for the entire mesh for implicit concentration solution	
{b _p }	vector of residuals for the entire mesh for pressure solution	
B _g	constant relating gas density to gas pressure	
C	mass concentration of tracer in fluid	(gm · gm ⁻¹ · fluid)
C _{oα}	solubility limit of species α	(gm · gm ⁻¹ · fluid)
\bar{D}_{ij}	components of dispersion tensor	(cm ² · s ⁻¹)
D _{αi}	molecular diffusivity of species α in fluid i	(cm ² · s ⁻¹)
J _α	mass flux of species α	
K _d	equilibrium sorption coefficient	(cm ³ · gm ⁻¹)
K _H	Henry's law coefficient	
L	length scale, such as typical particle size	(cm)
M _α	molecular weight of species α	(gm · mole ⁻¹)
N	total number of finite difference cells	
N _c	number of columns in the mesh	
N _r	number of rows in the mesh	
P	pressure	(dyne · cm ⁻²)
P _b	bubbling pressure	(dyne · cm ⁻²)
P _c	capillary pressure	(dyne · cm ⁻²)
P _e	Peclet number	
Q	kinetic sorption coefficient	(s ⁻¹)
R	universal gas constant	(erg · mole ⁻¹ · °C ⁻¹)
R _g	residual function for gas flow	
R _l	residual function for liquid flow	
S	mass source or sink	(gm · cm ⁻³ · s ⁻¹)
S _α	concentration of species adsorbed on matrix	(gm · gm ⁻¹ · solid)
S _m	maximum adsorption limit	(gm · gm ⁻¹ · solid)
T	temperature	(°C)
a _{l,jj}	longitudinal and transverse dispersivities	(cm)

TABLE I. Notation Used In TRACRN (cont'd)

Parameter	Description	Units
\bar{g}	gravity acceleration	(cm · s ⁻²)
f	gas saturation (σ_g)	
k	permeability	(darcys on input, converted to cm ² internally)
m_{ij}	coordinate system metric	
t	time	(s)
\vec{u}	mass velocity	(cm · s ⁻¹)
\vec{V}	pore velocity = \vec{u}/ϵ	(cm · s ⁻¹)
\vec{x}	spatial coordinate vector	(cm)
α	weighting factor for donor differencing of relative permeabilities	
α_c	coefficient for donor differencing of the transport equation	
α_v	curve fitting parameter in the van Genuchten relation for capillary pressure	(cm ⁻¹)
β	matrix compressibility	(cm ² /dyne)
γ	fluid compressibility	(cm ² /dyne)
ϵ	porosity	
λ	ln(2)/half-life of tracer	(s ⁻¹)
λ_v	curve fitting parameter in the van Genuchten/Mualem relations for relative permeability and capillary pressure	
μ	viscosity	(gm · cm ⁻¹ · s ⁻¹)
ρ	density	(gm · cm ⁻³)
σ	saturation	
σ_{to}	irreducible water saturation	
τ	pore-size index	
τ_c	constrictivity	
Ω	volume	(cm ³)
	(Subscripts)	
acc	acceptor cell	
don	donor cell	
f	refers to total fluid	
g	refers to gas phase	
i	refers to phase	
ijk	cell index number	
l	refers to liquid phase	
m	refers to matrix	
o	reference property	
q	cell face index	

TABLE I. Notation Used In TRACRN (cont'd)

Parameter	Description	Units
r	denotes relative permeability	
v	cell index number when considering entire mesh	
w	cell index number for cell v and its adjacent cells	
α	refers to chemical species α	
$\alpha - 1$	parent of species α (Superscripts)	
n	time level	
m	cell face index	
s	iteration counter	

For each tracer, the mass conservation equations are

$$\begin{aligned} \partial_t(\epsilon\sigma_i\rho_iC_\alpha) + \nabla \cdot (\rho_i\vec{u}_iC_\alpha) = \nabla \cdot (\epsilon\sigma_i\tau_c D_{\alpha i}\rho_i\nabla C_\alpha) + \epsilon C_\alpha S_i + \nabla \cdot [\epsilon\sigma_i\bar{D}_\alpha\nabla(\rho_iC_\alpha)] \\ - \epsilon\lambda_\alpha\sigma_i\rho_iC_\alpha + \epsilon\lambda_{\alpha-1}\sigma_i\rho_i\frac{C_{\alpha-1}}{M_{\alpha-1}}M_\alpha - \rho_i\rho_m[Q_{1\alpha}C_\alpha(S_{m\alpha} - S_\alpha) \\ - Q_{2\alpha}S_\alpha(C_{0\alpha} - C_\alpha)] \end{aligned} \quad (4)$$

and

$$\partial_t S_\alpha = Q_{1\alpha}C_\alpha(S_{m\alpha} - S_\alpha) - Q_{2\alpha}S_\alpha(C_{0\alpha} - C_\alpha) + \lambda_{\alpha-1}\frac{S_{\alpha-1}}{M_{\alpha-1}}M_\alpha - \lambda_\alpha S_\alpha \quad (5)$$

An arbitrary number of tracer species is allowed. The tracer concentrations are assumed to be small so that density and viscosity variations are negligible. Mass flow caused by the Soret effect has been ignored, as has diffusion in the solid phase. Equations (4) and (5) describe the advective/diffusive/dispersive transport of tracer species that can decay (in chains) and adsorb or desorb with mineral substrates. Several types of sorption models are allowed. In their full form, Eqs. (4) and (5) model saturable, nonequilibrium sorption. The rate of adsorption is represented by $Q_{1\alpha}$, and the rate of desorption is represented by $Q_{2\alpha}$. In Eq. (5), $S_{m\alpha}$ represents the maximum amount of tracer α that can adsorb onto a mineral substrate, whereas $C_{0\alpha}$ represents the solubility limit of tracer α . Transport under unsaturated conditions is also handled through the appearance of saturation σ_i in Eq. (4). By re-defining the C_α 's and S_α 's, colloid transport can also be modeled. For equilibrium sorption, Eqs. (4) and (5) are replaced with

$$\begin{aligned}
 \partial_t(\epsilon\sigma_i\rho_iC_\alpha) + \nabla \cdot (\rho_i\bar{u}_iC_\alpha) &= \nabla \cdot (\epsilon\sigma_i\tau_cD_{\alpha_i}\rho_i\nabla C_\alpha) \\
 &+ \epsilon C_\alpha S_i + \nabla \cdot [\epsilon\sigma_i\bar{D}_\alpha\nabla(\rho_iC_\alpha)] \\
 &- \epsilon\lambda_\alpha\sigma_i\rho_iC_\alpha + \epsilon\lambda_{\alpha-1}\sigma_i\rho_i\frac{C_{\alpha-1}}{M_{\alpha-1}}M_\alpha \\
 &- \rho_i\rho_m\left(K_{d\alpha}(\partial_tC_\alpha + \lambda_\alpha C_\alpha) - \lambda_{\alpha-1}C_{\alpha-1}\frac{M_\alpha}{M_{\alpha-1}}\right), \quad (6)
 \end{aligned}$$

where $K_{d\alpha}$ is an equilibrium sorption coefficient.

In Eqs. (4) and (6) a velocity-dependent dispersion tensor \bar{D}_α is used. Dispersion is a very complicated process. Measurements of dispersivity in the field show time and length scale effects. Some of this is simply related to scales of heterogeneity in the field geology and could, in principle, be computed by TRACRN. However, there appears to be a further effect that requires a better model (Gelhar 1986). Until a consensus is reached on the nature of that model, the current dispersion form will remain.

The conservation equations, Eqs. (1) through (6), involve quantities ($\rho_\ell, \rho_g, \sigma_\ell, \sigma_g, C_\alpha, \bar{u}_g, \bar{u}_\ell, S_\alpha$) that represent local volume averages. The averages are obtained by integrating the continuum conservation equations over small representative volumes (small compared with the scale of the problem at hand but large compared with the individual flow paths between the matrix grains). It is assumed that the concept of "representative elementary volume" is at least approximately valid for most soils and rocks. This averaging is necessary because our present mathematics cannot provide a practical means of solving the continuum equations at arbitrary points in such a complex system as a soil. Details of the averaging process and of the assumptions underlying Eqs. (1) through (6) can be found in Bear (1972).

An implicit assumption in Eqs. (4), (5), and (6) is that as a tracer moves into a small region of porous material from a neighboring region, the tracer is uniformly distributed throughout the pores and channels in that small region. This might not hold in all situations because fluid moves faster through the larger pores and channels. This will be a valid assumption if the characteristic diffusion time, say $t_D \simeq L^2/D_\alpha$, is about the same size as the characteristic residence time $\simeq \Delta x/V$ where Δx is the scale size of the region (or a computational grid size) and V is the pore velocity. In other words, if $V \leq \Delta x \cdot D_\alpha/L^2$ then the assumption is valid. For many soils and rocks, the characteristic pore size L will be a millimeter or less, and the condition will be satisfied for many instances. Another constraint exists. The flow law (given in Eq. (3)) is valid for Reynolds number ≤ 100 , that is, $\frac{LV\rho}{\mu} \leq 100$, or $V \leq \frac{100\mu}{\rho L} \simeq \frac{1}{L}$. This is usually not as restrictive as the former condition, however. Some tracer species, such as benzene and other organics, are volatile

and can move in both the liquid and air phases. (These compounds could be radioactive by containing C-14 for example.) TRACRN has the capability of calculating this two phase transport. Henry's law is used to partition a volatile tracer between the air and water phases, assuming local equilibrium.

Henry's law states

$$\rho_g C_v = K_H C_\ell \quad (7)$$

where C_v is concentration of the vapor in air, C_ℓ is the liquid concentration and K_H is Henry's coefficient.

The total amount of a tracer in a small volume $\Delta\Omega$ is then

$$\bar{C}_T = (\epsilon\sigma_\ell\rho_\ell C_\ell + (1-\epsilon)\rho_s K_d C_\ell + \epsilon\sigma_g\rho_g C_v)\Delta\Omega \quad (8)$$

The first term on the right hand side of Eq. (8) is the amount in the water phase, the second term represents the amount adsorbed onto the rock matrix, and the third term represents the vapor-air phase. Using Henry's law, we can write (8) as

$$\bar{C}_T = C_\ell [\epsilon(\sigma_\ell\rho_\ell + \sigma_g K_H) + \rho_s(1-\epsilon)K_d]\Delta\Omega = C_\ell \cdot A_H \cdot \Delta\Omega \quad (9)$$

Now the distribution between phases is expressed in terms of the liquid concentration. Similarly for the flux terms, we can write

$$\nabla \cdot (\rho_\ell C_\ell \vec{u}_\ell + \rho_g C_v \vec{u}_g) = \nabla \cdot [(\rho_\ell \vec{u}_\ell + K_H \vec{u}_g) C_\ell] \quad (10)$$

and

$$\begin{aligned} \nabla \cdot (\tau_c \epsilon \sigma_\ell \rho_\ell D_\ell \nabla C_\ell + \tau_c \epsilon \sigma_g \rho_g D_g \nabla C_v) \\ = \nabla \cdot [\tau_c \epsilon (\sigma_\ell \rho_\ell D_\ell + \sigma_g K_H D_g) \nabla C_\ell] \end{aligned} \quad (11)$$

Using (9), (10), and (11), the transport Eq. (6) for a volatile tracer becomes

$$\begin{aligned} \frac{\partial}{\partial t} (A_H C_\ell) + \nabla \cdot [(\rho_\ell \vec{u}_\ell + K_H \vec{u}_g) C_\ell] = \nabla \cdot [\tau_c \epsilon (\sigma_\ell \rho_\ell D_\ell + \sigma_g K_H D_g) \nabla C_\ell] \\ + \epsilon C_\ell S - \lambda A_H C_\ell \end{aligned} \quad (12)$$

2. Constitutive Relationships. In Eq. (3), k_i is a function of the saturated permeability of the matrix and of the degree of saturation of the pore space. It represents the exchange of momentum between the fluids and the drag on the fluids by the matrix. There are three options in TRACRN for calculating k_i : (1) use of Brooks-Corey (1964)

equations, (2) use of the van Genuchten (1978) and Mualem (1976) expressions, or (3) user supplied tables.

Brooks and Corey (1964) have derived expressions for k_i that give good agreement to data for many materials. They express the dependence of k_i on saturation with

$$k_\ell = k \cdot k_{\ell r}, \quad k_{\ell r} = \sigma_{\ell c}^{(3+2/\tau)} \quad (13)$$

and

$$k_g = k \cdot k_{gr}, \quad k_{gr} = (1 - \sigma_{\ell c})^2 [1 - \sigma_{\ell c}^{(1+2/\tau)}] \quad (14)$$

where k_ℓ is the liquid permeability, k_g is the permeability of the gas phase, k is the saturated permeability, and

$$\sigma_{\ell c} = \frac{(\sigma_\ell - \sigma_0)}{(1 - \sigma_0)} \quad (15)$$

Here σ_0 is the "irreducible" wetting saturation; that is, the minimum saturation at which continuous flow of the liquid phase can be maintained. It is a material property and depends on the soil or rock matrix pore structure and size. τ , the pore-size distribution index, is also a material property. Plots of k_{gr} and $k_{\ell r}$ are given in Figs. 1 and 2 respectively for different values of τ .

A second approach is to combine van Genuchten's relationship between saturation and matric potential (capillary pressure) with Mualem's equation for permeability as a function of matric potential, to produce an equation for permeability as a function of saturation:

$$k_\ell = k \cdot k_{\ell r}, \quad k_{\ell r} = \sqrt{\sigma_{\ell c}} \{1 - (1 - \sigma_{\ell c}^{1/\lambda_v})^{\lambda_v}\}^2 \quad (16)$$

$$k_g = k \cdot k_{gr}, \quad k_{gr} = 1 - k_{\ell r} \quad (17)$$

Eq. (16) is the composite of Mualem's and van Genuchten's equations for water permeability. Eq. (17) is an approximation to air permeability (Mualem only described liquid phase permeability).

Alternatively, k_i can be represented as a tabular function of saturation if the forms of Eqs. (13) and (14) or (16) and (17) are not convenient for a particular application, or if saturated air permeability is significantly different from saturated water permeability. The permeability k can be anisotropic as long as the principal axes of the permeability tensor coincide with the coordinate axes. [However, for anisotropic media, the form used for the

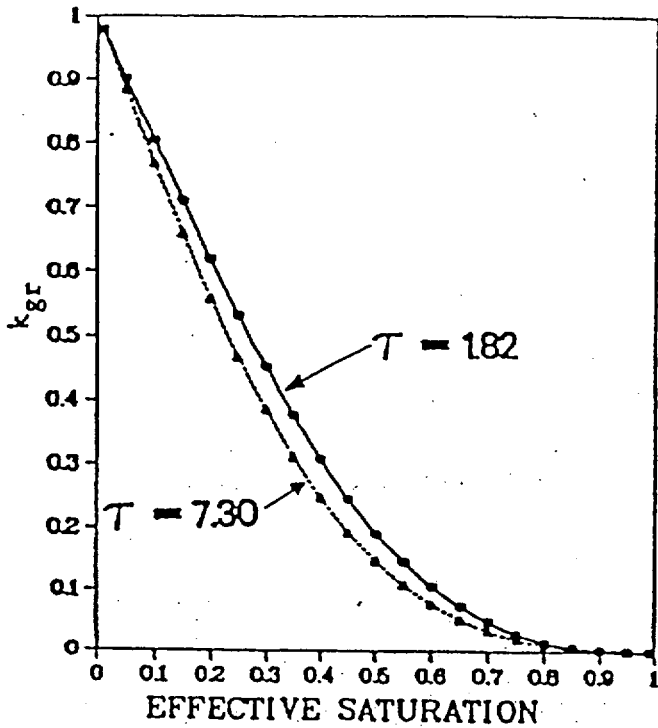


Fig. 1. Relative air permeability for $\tau=1.82$ and $\tau = 7.30$

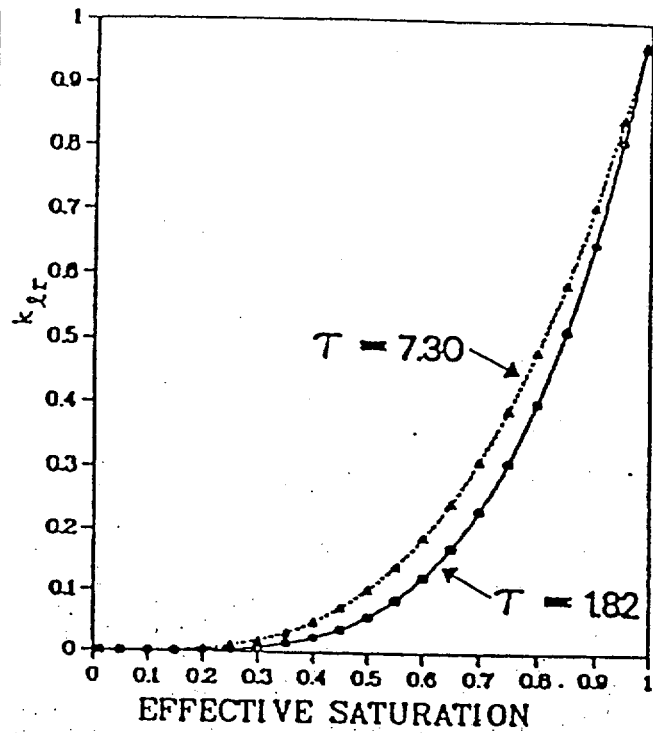


Fig. 2. Relative water permeability for $\tau = 1.82$ and $\tau = 7.30$

dispersion tensor may not be correct. Also, the relative permeabilities k_{lr} and k_{gr} as given in Eqs. (13) and (14) and (16) and (17) do not exhibit any directional dependence.]

An equation of state is needed. The ideal gas law is assumed

$$P_g = \rho_g / B_g, \text{ where } B_g = \frac{M_g}{R(T + 273.15)} \quad (18)$$

The liquid is considered slightly compressible for saturated conditions. That is,

$$\rho_l = \rho_{l0} [1 + \gamma(P - P_0)] \quad (19)$$

where P_0 is a reference pressure. In unsaturated flow, ρ_l will usually be much less compressible than ρ_g , and so is treated as incompressible when $\sigma_l < 1$.

Liquid pressure P_l , gas pressure P_g and matrix suction P_c are related by

$$P_l = P_g - P_c(\sigma_l) \quad (20)$$

As with relative permeabilities, there are three options for P_c : (1) a Brooks-Corey (1964) model, (2) a van Genuchten (1978) equation, or (3) user supplied tables. Brooks and Corey (1964), on the basis of a large number of drainage experiments, found that capillary pressure could be represented well by the expression

$$P_c = P_b \sigma_{\ell c}^{-1/\tau} \quad (21)$$

where τ and P_b are material constants. Our convention is that P_c is ≥ 0 ; τ is called the "pore-size distribution index"; P_b , the bubbling pressure, is the minimum value of P_c on the drainage curve just before P_c drops to zero. P_c increases without limit as $\sigma_{\ell c} \rightarrow 0$ in Eq. (21). We limit P_c by not allowing $\sigma_{\ell c}$ to decrease below 10^{-2} ; physically, this corresponds to limiting the smallest pore size that contributes to P_c . For $\sigma_{\ell c} < 0.01$, we artificially define P_c to increase linearly to a value at $\sigma_{\ell} = 0$ which is two times the value of P_c at $\sigma_{\ell c} = 0.01$. Table II (Brooks and Corey 1964) gives some typical values for the material parameters P_b , τ , and σ_0 .

TABLE II
TYPICAL VALUES FOR MATERIAL PROPERTIES

	P_b (bars)	τ	σ_0 ^{Swi}
Fine sand	0.0310	7.30	0.50
"Volcanic" sand	0.0756	1.82	0.20
Glass beads	0.0414	3.70	0.15
Silt loam	0.0162	2.29	0.60

In the second option, van Genuchten's relation is used for P_c , i.e.,

$$P_c = \frac{\rho g}{\alpha_v} \left\{ \sigma_{\ell c}^{-1/\lambda_v} - 1 \right\}^{(1-\lambda_v)} \quad (22)$$

The third option requires the user to supply a table of P_c vs σ_g for those materials for which (21) or (22) are not applicable.

An additional requirement is that

$$\sigma_g + \sigma_{\ell} = 1 \quad (23)$$

Porosity ϵ is allowed to vary with pressure. Dynamic changes in porosity can have a dramatic effect on flow because storage capacity and permeability are generally quite sensitive to changes in porosity. A simple linear relation is used:

$$\epsilon = \epsilon_o[1 + \beta(P - P_o)] \quad (24)$$

Permeability is strongly sensitive to porosity changes. In TRACRN, we use

$$k = k_o \left(\frac{\epsilon}{\epsilon_o} \right)^2 = k_o[1 + \beta(P - P_o)]^2 \quad (25)$$

where k_o is saturated permeability at reference pressure.

There are three options for evaluating dispersion. The first uses a full tensor form. The dispersion tensor (Bear 1972) is given by

$$\bar{\bar{D}}_{\alpha ij} = \left[a_{II} |\bar{V}| m_{ij} + \frac{(a_I - a_{II})V_i V_j}{|\bar{V}|} \right] q(P_c) \quad (26)$$

and

$$q(P_c) = \frac{P_c}{P_c + 6} \quad (27)$$

where

$$P_c = \frac{L |\bar{V}|}{D_\alpha} \quad (28)$$

and

$$\bar{V} = \frac{\bar{u}}{\epsilon} \quad (29)$$

Here, L is a (user-supplied) length scale, a_I is the longitudinal dispersivity coefficient and a_{II} is the transverse dispersivity coefficient. A simplified version of dispersion uses only the diagonal terms of Eq. (26). A third option for dispersion allows the user to specify dispersion coefficients in the x -, y - and z - directions for each material. In this case, the dispersion tensor only has diagonal terms and is computed from $\bar{\bar{D}}_\alpha = \bar{d} \bar{V}$, with $d_{ijk} = 0$ for $i \neq j \neq k$. For the second and third options, we are assuming that the dispersion principal axes coincide with the x -, y -, and z - axes.

Finally, the diffusivities of solutes are strongly attenuated for unsaturated conditions. We use

$$D = D_o a e^{-b\sigma} \quad (30)$$

where D_o is the diffusivity at full saturation and a and b are material dependent.

Several additional relations are needed to complete the model:

$$\tau = \tau(\bar{x}), \sigma_{\ell 0} = \sigma_{\ell 0}(\bar{x}), P_b = P_b(\bar{x}), k = k(\bar{x}), \rho_m = \rho_m(\bar{x}) \quad (31)$$

and

$$Q_{1\alpha} = Q_{1\alpha}(\bar{x}), Q_{2\alpha} = Q_{2\alpha}(\bar{x}), L = L(\bar{x}), S_{m\alpha} = S_{m\alpha}(\bar{x}), C_{0\alpha} = C_{0\alpha}(\bar{x}) \quad (32)$$

These are all indicated and defined in the list of namelist input variables.

Boundary conditions on all boundaries have the form

$$s(X_B)G(t) + r(X_B)\frac{\partial G}{\partial n} = f(t, X_B) \quad (33)$$

where G represents $P_g, P_\ell, \sigma_g, \sigma_\ell$ or C_α ; X_B represents points on the boundary; $\frac{\partial}{\partial n}$ represents the derivative normal to the boundary; $s = 0$ or 1 , $r = 1$ or 0 , at each boundary point as specified by the user; and $f(t, X_B)$ is an arbitrary user-supplied function. At time $= 0$, the spatial distribution of C_α, σ_g and P are required also.

Equations (1) through (33) constitute the TRACRN model. They allow calculation of transient, fully two-phase flow with tracer transport in a heterogeneous material that is nonuniform, porous, and permeable. This equation set is solved numerically as described in Sec. 3 below.

3. Numerical Model. The TRACRN code was written with flexibility and ease of use in mind. Equations (1) through (33) are solved for one, two, or three dimensions using either Cartesian or cylindrical coordinates. We assume a unique, well-behaved solution to Eqs. (1) through (33) exists for all physically reasonable boundary conditions and initial conditions. This confidence results from experience with many problems where the numerical solution of the difference equations matches closely one of the few analytic solutions available or agrees with experimental data. Moreover, the fact that solutions agree with experimental data gives us confidence that Eqs. (1) through (33) reasonably approximate the true physical situation for many applications.

The region of interest is represented by a computational mesh of cells or zones. Figure 3 shows examples of a Cartesian and a cylindrical mesh with a corresponding single finite difference cell. The rows, columns, and layers of cells need not be equally spaced. Some variables (pressure, density, concentration, and saturation) are evaluated at cell centers; others (velocity and permeability components) are evaluated at cell interfaces. Different numbering systems are used in TRACRN for 3-dimensional and 2-dimensional

grids. A 1-dimensional problem is represented using a 3-dimensional grid. The cell number is represented by the variable "ijk".

Figure 4 shows a typical 3-dimensional grid in rectangular coordinates. There are m internal zones in the x-direction, q internal zones in the y-direction, and n internal zones in the z-direction. In each of the three directions there are two boundary zones with no thickness making a total of m2 (= m + 2) zones in the x-direction, q2 (= q + 2) zones in the y-direction, and n2 (= n + 2) zones in the z-direction. The origin (first cell) is in the front, left, bottom corner, which is a boundary cell. The cell number increases first by traveling down a row (in the +y-direction), then by moving left to the front of the next column (in the +x-direction), and traveling down that row. Once all cells in a layer are numbered, the cells in the next layer (in the +z-direction) are numbered starting again in the front, left corner. The numbering system includes the boundary cells, making a total of m2q2n2 (= m2 x q2 x n2) cells. Figure 4 shows the value of "ijk" for a few cells. For a 1-D vertical problem, m = q = 1 so m2 = q2 = 3.

Figure 5 shows a typical 2-D grid in rectangular coordinates. Again there are m internal zones and m2 total zones in the x-direction, and n internal zones and n2 total zones in the z-direction. The y-direction is not included. For a 2-D grid, the first cell is the bottom left boundary cell and the zone number increases by traveling up a layer (in the +z-direction), then by moving right to the bottom of the next column (in the +x-direction). The numbering system includes the boundary cells making a total of m2n2 (= m2 x n2) cells. Figure 5 shows the cell number for a few of the cells.

The partial differential equations of the model are approximated by finite difference algebraic equations, one set for each computational cell. These difference equations relate dependent variable values at different discrete spatial locations and at different times. An approximate solution to Eqs. (1) through (33) is obtained by marching forward in time, solving the simultaneous set of difference equations for all cells at each time value.

a. Numerical Solution for Flow. The equations describing unsaturated air and water flow are solved using an implicit finite difference numerical method. The partial differential equations for conservation of mass are coupled with a Darcy's law formulation for low Reynolds number laminar flow and a Forchheimer law for Reynolds numbers between 1 and 100 (inertial flow). These equations are discretized on a rectangular grid. The temporal discretization is a fully implicit backward differencing; the spatial discretization uses the donor cell method for relative permeability terms and a harmonic averaging for the intrinsic (saturated) permeability. Pressure and saturation are evaluated at grid cell centers, while velocity components are computed at grid cell face centers.

The equation for water transport is

$$\frac{\partial}{\partial t}(\epsilon \rho_l \sigma_l) + \nabla \cdot (\rho_l \bar{u}_l) = \epsilon S_l \quad (34)$$

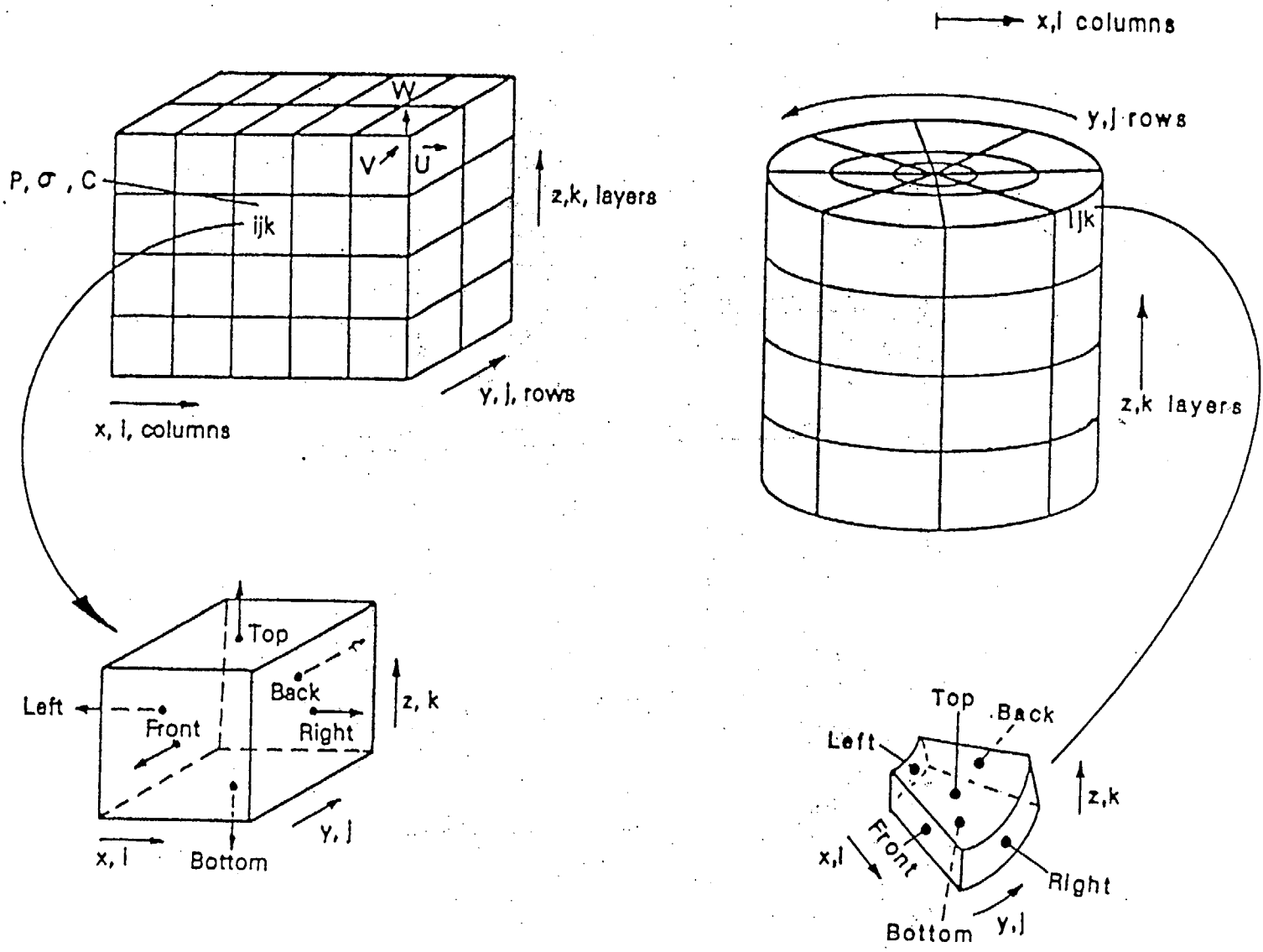


Fig. 3. Typical computational mesh in Cartesian coordinates, and cylindrical coordinates.

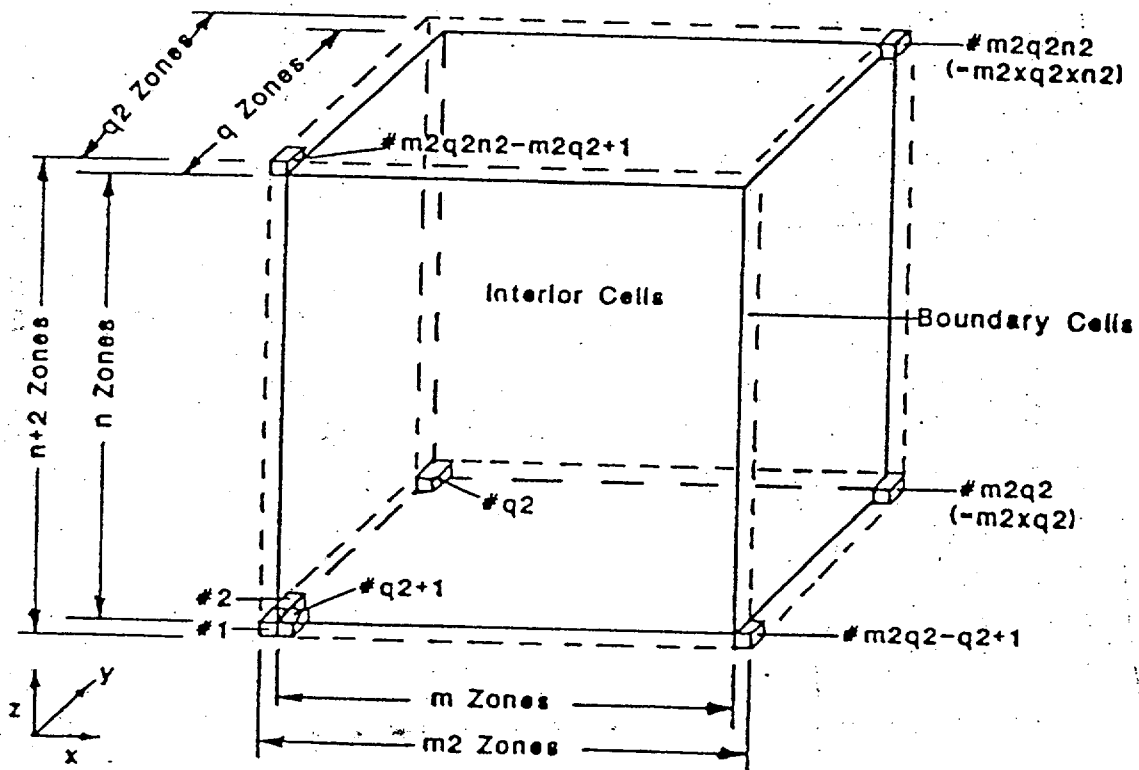


Fig. 4. Typical 3-dimensional rectangular grid.

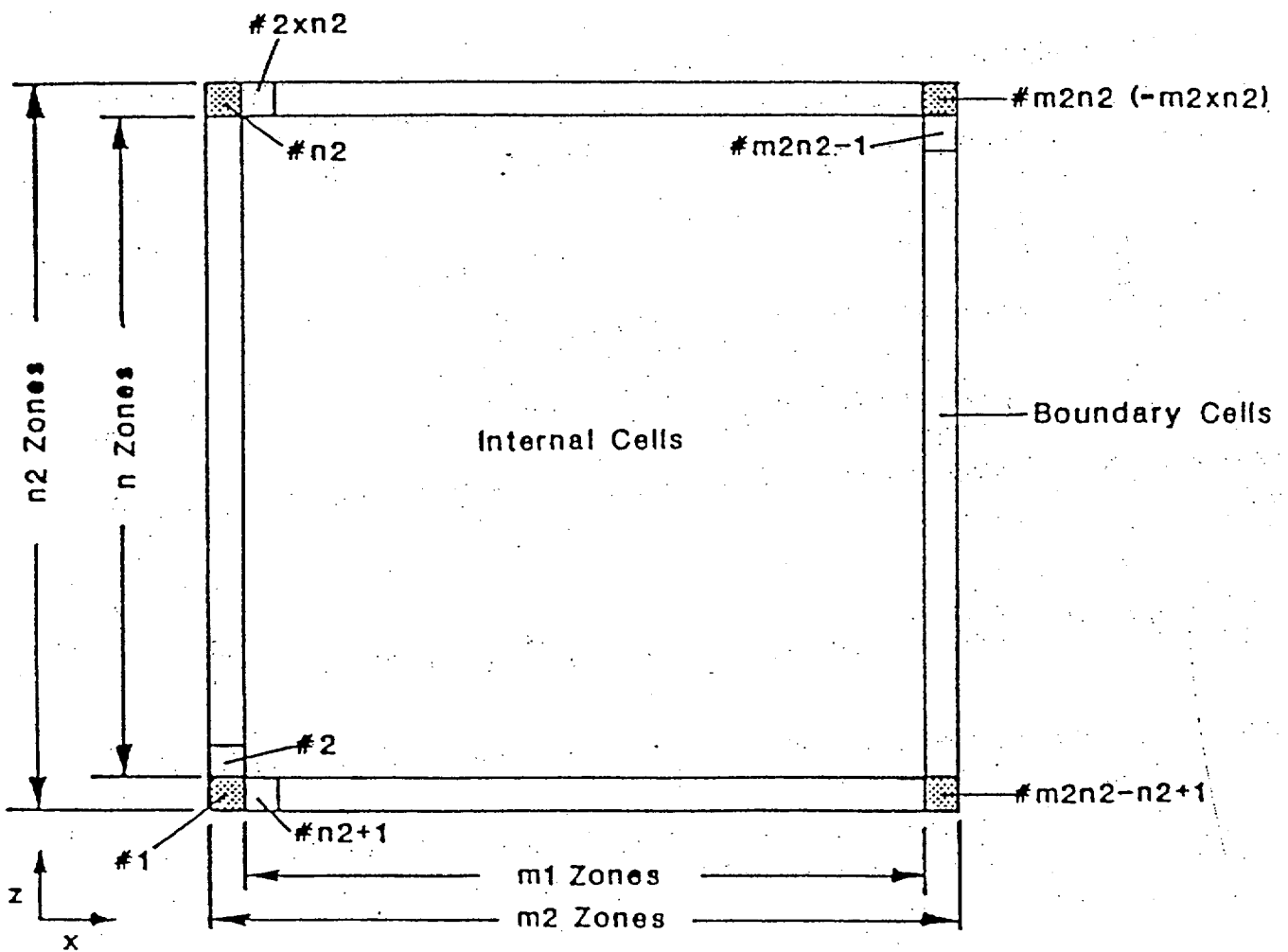


Fig. 5. Typical 2-dimensional rectangular grid.

where

$$\epsilon = \epsilon_o((1 - \beta P_o) + \beta P) = \epsilon_o \bar{\epsilon}(P) , \quad (35)$$

$$\rho_\ell = \rho_{\ell o}((1 - \gamma P_o) + \gamma P) = \rho_{\ell o} \bar{\rho}_\ell(P) ; \quad (36)$$

$$\bar{u}_\ell = -\frac{\bar{k}}{\mu_\ell} (\alpha k_{\ell r_{don}} + (1 - \alpha) k_{\ell r_{acc}}) (\nabla P_\ell + \rho_\ell \hat{g}) , \quad (37)$$

and

$$\sigma_\ell = \sigma_\ell(P_\ell), \quad k_{\ell r} = k_{\ell r}(P_\ell) . \quad (38)$$

The velocity dependent term in Forchheimer's equation (Eq. (3)) is included in Eq. (37) through the variable k using the velocity calculated at the last time step.

Equation (34) is integrated over each grid cell volume to give Eq. (39).

$$\int_{\Omega_{ijk}} \frac{\partial(\epsilon \rho_\ell \sigma_\ell)}{\partial t} d\Omega + \int_{\Omega_{ijk}} \nabla \cdot (\rho_\ell \bar{u}_\ell) d\Omega = \int_{\Omega_{ijk}} \epsilon \dot{S}_\ell d\Omega \quad (39)$$

By use of the divergence theorem, we can rewrite Eq. (39):

$$\frac{\partial}{\partial t} \int_{\Omega_{ijk}} \epsilon \rho_\ell \sigma_\ell d\Omega + \int_{\partial\Omega_{ijk}} \rho_\ell \bar{u}_\ell \cdot dA = \int_{\Omega_{ijk}} \epsilon \dot{S}_\ell d\Omega. \quad (40)$$

Application of the finite differencing algorithm yields the following approximation to Eq. (40):

$$\left(\frac{(\epsilon \rho_\ell \sigma_\ell)^{(n+1)} - (\epsilon \rho_\ell \sigma_\ell)^{(n)}}{\Delta t} \right) \Delta\Omega_{ijk} + \sum_{q=1}^6 \langle \rho_\ell \rangle \bar{u}_\ell^{(n+1)} \Delta A (-1)^q = \epsilon_o \dot{S}_\ell \Delta\Omega_{ijk} \quad (41)$$

where the superscript refers to time level n or $n+1$ and the symbol $\langle \rangle$ refers to a spatially averaged term.

At a given time level (n), we assume that the pressure P_ℓ and saturation σ_ℓ are known in each computational cell. The values of P_ℓ and σ_ℓ are required at time level ($n+1$). Equation (41) with Eqs. (35)-(38) are used to find $P_\ell^{(n+1)}$. The equations are solved iteratively via a Newton-Raphson iteration (the dependence of σ_ℓ and $k_{r\ell}$ on pressure make Eq. 41 nonlinear). Currently pure donor cell weighting of the relative permeabilities is used (i.e., $\alpha = 1$) in Eq. (37).

First a residual function is defined:

$$R_{\ell,ijk}^{(n+1,s+1)} = \epsilon_o \rho_{\ell o} \frac{\Delta\Omega_{ijk}}{\Delta t} \left(\bar{\epsilon}^{(n+1,s+1)} \bar{\rho}_\ell^{(n+1,s+1)} \sigma_\ell^{(n+1,s+1)} - \bar{\epsilon}^{(n)} \bar{\rho}_\ell^{(n)} \sigma_\ell^{(n)} \right)_{ijk}$$

$$\begin{aligned}
 & -\epsilon_0 \dot{S}_\ell \Delta \Omega_{ijk} - \frac{\rho_{\ell 0}}{\mu_\ell} \sum_{q=1}^6 \Delta A_{qijk} \langle \bar{\rho}_\ell \rangle_q \bar{k}_q \left(\alpha k_{\ell r_{don}}^{(n+1,s+1)} \right. \\
 & \left. + (1-\alpha) k_{\ell r_{acc}}^{(n+1,s+1)} \right) \left(\frac{P_{\ell q}^{(n+1,s+1)} - P_\ell^{(n+1,s+1)}}{\Delta x_q} + \frac{g}{2} \rho_\ell^{(n+1,s+1)} \bar{z} \right)_{ijk} \quad (42)
 \end{aligned}$$

where the superscript represents the quantity value at the $s + 1^{th}$ iteration. An exact solution of the finite difference Eq. (41) would result in $R_{\ellijk}^{(n+1)} = 0$ for every cell (ijk) . Because of the iterative nature of our solution to (41), we will ordinarily not be able to achieve this. However, use of the Newton-Raphson iteration with a good starting guess for the solution will allow us to reduce $|R_{\ellijk}|$ to a small value in every cell (ijk) in only a few iterations. The procedure is simple in principle - expand $R_{\ellijk}^{(n+1,s+1)}$ in a Taylor series around $P_\ell^{(n+1,s)}, \sigma_\ell^{(n+1,s)}$, keep only 1st order terms, and solve the resulting matrix equation, and repeat for successive iterations until $|R_{\ellijk}^{(n+1,s+1)}| < \text{tolerance}$ for every (ijk) . (See section e.)

$$\begin{aligned}
 R_{\ellijk}^{(n+1,s+1)} & \approx R_{\ellijk}^{(n+1,s)} + \sum_w \frac{\partial R_{\ellijk}^{(n+1,s)}}{\partial P_{\ell w}} \delta P_{\ell w}^{(n+1,s+1)} + \sum_w \frac{\partial R_{\ellijk}^{(n+1,s)}}{\partial \sigma_{\ell w}} \delta \sigma_{\ell w}^{(n+1,s+1)} \\
 & = R_{\ellijk}^{(n+1,s)} + \sum_w \left(\frac{\partial R}{\partial P_{\ell w}} - \frac{\partial R}{\partial \sigma_{\ell w}} \frac{d\sigma_{\ell w}}{dP_c} \right)_{ijk}^{(n+1,s)} \delta P_{\ell w}^{(n+1,s+1)} \\
 & = R_{\ellijk}^{(n+1,s)} + \sum_w \left(\frac{dR_\ell}{dP_\ell} \right)_{ijkw}^{(n+1,s)} \delta P_{\ell w}^{(n+1,s+1)} \quad (43)
 \end{aligned}$$

where subscript w ranges over all the cell faces. The term involving $\delta \sigma_\ell$ was removed by making use of the relation $P_c(\sigma_\ell) = P_g - P_\ell$ which implies that $\delta \sigma_\ell = \frac{d\sigma_\ell}{dP_c} (\delta P_g - \delta P_\ell) = \frac{d\sigma_\ell}{dP_c} \delta P_\ell$ since here it is assumed that $\delta P_g = 0$. We then solve

$$[A] \{ \delta P_\ell \} = \{ b_p \}_\ell, \quad P_\ell^{(n+1,s+1)} = P_\ell^{(n+1,s)} + \delta P_\ell^{(n+1,s+1)}, \quad (44)$$

where

$$\{ b_p \}_\ell = -R_{\ellijk}^{(n+1,s)}, \quad [A] = \left(\frac{\partial R_{\ellijk}}{\partial P_w} \right)^{(n+1)} \quad (45)$$

The derivative of R with respect to P is defined numerically as follows (now the subscript of ijk is replaced by a single subscript v which ranges between 1 and N where $N = \text{total number of cells}$):

$$\begin{aligned} \frac{\partial R_v^{(n+1,s)}}{\partial P_w} &\approx -\frac{\rho_{t0}}{\mu_t} \Delta A_w \bar{k}_w \left(\alpha k_{lr_{don}}^{(n+1,s)} + (1-\alpha) k_{lr_{acc}}^{(n+1,s)} \right) < \bar{\rho}_t > \\ &\times \left(\frac{1}{\Delta x_w} + \frac{g}{2} \hat{z} \rho_{t0} \gamma \right) - \frac{\rho_{t0}}{\mu_t} \Delta A_w \bar{k}_w \left(\alpha \frac{dk_{lr_{don}}^{(n+1,s)}}{dP_w} + (1-\alpha) \frac{dk_{lr_{acc}}^{(n+1,s)}}{dP_w} \right) \\ &\times \left(\frac{P_{t_w}^{(n+1,s)} - P_{t_v}^{(n+1,s)}}{\Delta x_w} + \frac{\hat{g}}{2} \hat{z} \bar{\rho}_{t_w}^{(n+1,s)} \right) \end{aligned} \quad (46)$$

for $w = v \pm 1$, $w = v \pm N_c$ and $w = v \pm N_c \cdot N_r$, where N_c = number of columns in the mesh and N_r = number of rows. For $w = v$,

$$\begin{aligned} \frac{dR_v^{(n+1,s)}}{dP_w} &\approx \epsilon_o \rho_{t0} \frac{\Delta \Omega_v}{\Delta t} \left(\beta \bar{\rho}_t^{(n+1,s)} \sigma_t^{(n+1,s)} + \bar{\epsilon}^{(n+1,s)} \gamma \sigma_t^{(n+1,s)} \right. \\ &\left. + (\bar{\epsilon} \bar{\rho})_t^{(n+1,s)} \frac{d\sigma_t^{(n+1,s)}}{dP_{t_v}} \right)_v - \frac{\rho_{t0}}{\mu_t} \sum_{q=1}^6 \Delta A_{qv} < \bar{\rho}_{lqv} > \bar{k}_{qv} (\alpha k_{lr_{don}}^{(n+1,s)} \\ &+ (1-\alpha) k_{lr_{acc}}^{(n+1,s)})_v \left(\frac{-1}{\Delta x_q} + \frac{g}{2} \hat{z} \gamma \right)_v - \frac{\rho_{t0}}{\mu_t} \sum_{q=1}^6 \Delta A_{qv} \bar{k}_{qv} \\ &\times \left(\alpha \frac{\partial}{\partial P_w} (\bar{\rho}_{lq} k_{lr_{don}})^{(n+1,s)} + (1-\alpha) \frac{\partial}{\partial P_w} (\bar{\rho}_{lq} k_{lr_{acc}})^{(n+1,s)} \right) \\ &\times \left(\frac{P_{lq} - P_t}{\Delta x_q} + \frac{\hat{g}}{2} \bar{\rho}_t \right)_v^{(n+1,s)} \end{aligned} \quad (47)$$

(In the TRACRN code, capillary pressure and relative permeabilities are given as functions of air saturation. Consequently terms such as $\frac{d\sigma_t}{dP_t}$ are replaced by $-\frac{df}{dP_t}$ (f = air saturation = $\sigma_g = 1 - \sigma_t$) and $\frac{dk_{lr}}{dP_t} = \frac{dk_{lr}}{df} \frac{df}{dP_t}$. Eq. (44), with coefficients defined by Eqs. (46) and (47), provides a solution to unsaturated water flow in which air movement and air compressibility are ignored.

A completely analogous approach is used to solve for air pressure in situations in which only air movement is considered. In this case, the conservation equation is

$$\frac{\partial(\epsilon \sigma_g \rho_g)}{\partial t} + \nabla \cdot \rho_g \bar{u}_g = \epsilon_o \dot{S}_g \quad (48)$$

where

$$\rho_g = B_g P_g, \quad B_g = \text{const.} \quad (49)$$

and

$$\bar{u}_g = -\frac{k_g}{\mu_g}(\nabla P_g + \rho_g \hat{g}) \quad (50)$$

Using a fully implicit, backward time finite differencing leads to an equation similar to Eq. (41):

$$\left(\sigma_g^{(n+1)} \bar{\epsilon}^{(n+1)} P_g^{(n+1)} - \sigma_g^{(n)} \bar{\epsilon}^{(n)} P_g^{(n)} \right)_{ijk} \left(\frac{\epsilon_o \Delta \Omega}{\Delta t} \right)_{ijk} - \sum_{q=1}^6 \frac{k_{gq}}{\mu_g} \left(\frac{P_{gq}^2 - P_g^2}{2 \Delta x_q} + \frac{B_{gg}}{2} (P_g + P_{gq})^2 \right)_{ijk}^{(n+1)} \Delta A_q = \epsilon_o \frac{S_g}{B_g} \Delta \Omega_{ijk} \quad (51)$$

As before, Eq. (51) is nonlinear for P_g , air pressure, and must be solved iteratively. A residual is defined

$$R_{g_{ijk}}^{(n+1,s+1)} = \left(\sigma_g^{(n+1,s+1)} \bar{\epsilon}^{(n+1,s+1)} P_g^{(n+1,s+1)} - \sigma_g^{(n)} \bar{\epsilon}^{(n)} P_g^{(n)} \right)_{ijk} \frac{(\epsilon_o \Delta \Omega)_{ijk}}{\Delta t} - \epsilon_o \frac{S_g}{B_g \Delta \Omega_{ijk}} - \sum_{q=1}^6 \Delta A_q \frac{k_{gq}}{\mu_g} \left(\frac{P_{gq}^2 - P_g^2}{2 \Delta x_q} + \frac{B_g}{2} (P_g + P_{gq})^2 \right)_{ijk}^{(n+1,s+1)} \quad (52)$$

where $k_{gq} = (\alpha k_{gr_{aon}} + (1 - \alpha) k_{gr_{acc}}) \bar{k}_q$ and where k_{gq} is the effective permeability at interface q in cell (ijk) . k_{gq} is a function of saturation, so may vary spatially, but will not vary temporally because for this option (IFLOW=1), the water phase doesn't move (i.e., $\sigma_g^{(n+1)} = \sigma_g^{(n)}$).

As before, R is expanded in a Taylor series and truncated after the 1st derivative terms.

$$\begin{aligned} R_{g_i}^{(n+1,s+1)} &\cong R_{g_i}^{(n+1,s)} + \sum_j \frac{\partial R_{g_i}}{\partial P_{gj}} \delta P_g^{(n+1,s+1)} + \sum_j \frac{\partial R_{g_i}}{\partial \sigma_{gj}} \delta \sigma_{gj}^{(n+1,s+1)} \\ &= R_{g_i}^{(n+1,s)} + \sum_j \frac{\partial R_{g_i}}{\partial P_{gj}} \delta P_g^{(n+1,s+1)} \end{aligned} \quad (53)$$

(We are assuming $\delta \sigma_g = 0$ here.)

We want $R_{g_i}^{(n+1,s+1)} = 0$. So (53) becomes

$$-R_{g_i}^{(n+1,s)} = \sum_j \left(\frac{\partial R_{g_i}}{\partial P_{g_j}} \right)^{(n+1,s)} \delta P_{g_j}^{(n+1,s+1)} \quad (54)$$

which is solved for $\delta P_g^{(n+1,s+1)}$. Then $P_g^{(n+1,s+1)} = P_g^{(n+1,s)} + \delta P_g^{(n+1,s+1)}$. The coefficients $\frac{\partial R_i}{\partial P_{g_j}}$ are given for $i \neq j$

$$\frac{\partial R_{g_i}}{\partial P_{g_j}} = -\frac{\Delta A_{iq} k_{gij}}{\mu_g \Delta x_{ij}} \left(P_{g_j} + \Delta x_{ij} g_{ij} B_g (P_{g_i} + P_{g_j}) \right)^{(n+1,s)} \quad (55)$$

and for $i = j$

$$\begin{aligned} \frac{\partial R_{g_i}}{\partial P_{g_j}} = & \left(\varepsilon^{(n+1,s)} + \beta P_g^{(n+1,s)} \right) \left(\frac{\varepsilon_o f \Delta \Omega_{ijk}}{\Delta t} \right) \\ & + \sum_{q=1}^6 \frac{\Delta A_{ij} k_{g iq}}{\mu_g \Delta x_{iq}} \left(P_{g_i} - B_g g_{iq} \Delta x_{iq} (P_{g_i} + P_{g_q}) \right)^{(n+1,s)} \end{aligned} \quad (56)$$

In (55) and (56), we have assumed that $\sigma_g^{(n+1)} = \sigma_g^{(n)}$ and so $\frac{\partial}{\partial \sigma_g} = 0$.

For two-phase flow in which both air and water movement are important, Eq. (44) is solved for water pressure at each time step. Then when the iteration for water pressure has converged, Eq. (54) is iterated (using latest values of saturation to calculate k_g 's) to convergence for air pressure P_g . Since the equations for air and water are not fully coupled, it will not be robust for every situation, but will work well for some problems. Full two-phase flow is implemented in the TRACR3D code (Travis 1984).

b. Numerical Solutions for Transport. An important feature of the TRACRN code is its ability to compute transient, three-dimensional transport of reactive chemical species. Currently, TRACRN can model transport of an arbitrary number of chemical tracers with the following features: advection, molecular diffusion, mechanical dispersion, radioactive decay (an n-chain decay is allowed), and a choice of sorption models [simple K_d equilibrium sorption, Eq. (6), or a nonequilibrium saturable sorption model, Eq. (4)]. The nonequilibrium model can be run in an unsaturable mode ($S_{m\alpha}$ large) and an irreversible ($Q_{2\alpha} = 0$) as well as reversible ($Q_{1\alpha} \neq 0$, $Q_{2\alpha} \neq 0$) mode. Movement of tracers can also occur in both phases via Henry's law. Some tracers, especially organics such as benzene, will partition between the liquid and air phases. Henry's law is a reasonable approximation when local equilibrium holds. The actual number of tracers that can be handled is restricted by computer memory size. Updating of tracer concentrations occurs after flow variables and velocities have been advanced.

Accurate solution of the transport equation for solutes in 1- or 2-phase porous flow can be a difficult goal to achieve. For moderate to high Peclet number $\left(P_c = \frac{LV}{D}\right)$ situations, very steep concentration fronts typically develop. Numerical resolution of such steep profiles requires either (1) very small mesh subdivisions, (2) high order approximations, or (3) a moving mesh with a region of fine divisions which follow the steep portions of the concentration field. TRACRN uses several approaches depending on the particular transport processes being considered. There is an option to use an implicit, fast finite difference solution for transport of adsorbing, radioactive species. This option uses a simple backward-time, variable donor cell space differencing. Dispersion cannot have its full tensor form, but only diagonal terms. This method is especially efficient for transport through a steady velocity field.

Under this option (ISOLVC=1), a numerical solution of Eq. (12) is obtained. Transport by advection, diffusion and dispersion are allowed, along with equilibrium, reversible sorption and radioactive decay. Transport in both phases is possible via Henry's law. Dispersion is limited to option three, i.e., the dispersion tensor's only non-zero entries are on the diagonal and are user-supplied. The numerical solution is computed by a simple, backward-time, weighted donor finite difference approximation to Eq. (12), namely,

$$\left[(A_H C_\ell)_{ijk}^{n+1} - (A_H C_\ell)_{ijk}^n \right] \frac{\Delta \Omega_{ijk}}{\Delta t} + \sum_{q=1}^6 \left[\langle B_H \rangle_q^{n+1} \Delta A_q (\alpha_c C_{\ell,ijk} + (1 - \alpha_c) C_{\ell,q})^{n+1} (-1)^q \right]_{ijk} \\ = \sum_{q=1}^6 (C_{\ell,q}^{n+1} - C_{\ell,ijk}^{n+1}) \frac{\Delta A_q}{\Delta x_q} D_{Hq}^{n+1} + \epsilon S C_{\ell,ijk} \Delta \Omega_{ijk} - \lambda A_{Hijk}^{n+1} C_{\ell,ijk}^{n+1} \Delta \Omega_{ijk} \quad (57)$$

where q ranges over the cell faces of cell ijk , and

Additional terms to be used constant

$$A_H = \epsilon(\sigma_\ell \rho_\ell + \sigma_g K_H) + (1 - \epsilon)\rho_s K_d, \quad (58)$$

$$B_H = \rho_\ell \vec{u}_\ell + K_H \vec{u}_g, \quad (59)$$

$$D_H = \epsilon \tau_c (\rho_\ell \sigma_\ell D_\ell + K_H D_g), \quad (60)$$

and α_c (CDONOR) ranges from 0.5 (centered space differencing) to 0 (pure donor). The quantities A_{Hijk} , B_{Hijk} and D_{Hijk} are evaluated after the flow variables (pressure, saturation and velocity) have been updated.

Equation (57) represents a set of linear algebraic equations for the concentration at each cell center, and can be written as

$$[A_c] \{C_c^{n+1}\} = \{b_c\} \quad (61)$$

where $[A_c]$ is a sparse banded matrix which does not depend on C_t . For 1-D situations, $[A_c]$ is a tridiagonal matrix; in 2-D it has 5 bands and for 3-D problems it is 7-banded. Boundary conditions are easily incorporated into Eq. (61); they result in modified entries for certain rows and columns of $[A_c]$ and corresponding entries in $\{b_c\}$. Since Eq. (61) is linear, no iteration is required, in contrast to the flow equations. Equation (61) is solved using the same incomplete factorization method employed at each iteration of the flow equations, (see Section c below). This implicit solution does not use either the "sharp" donor or tensor anti-diffusion techniques available under the explicit solution option (ISOLVC=0) to reduce numerical diffusion. However, it is very fast, unconditionally stable, and reasonably accurate if (1) adequate mesh zoning is used, or (2) dispersion/diffusion processes are significant relative to advection, or (3) material or other properties are not known precisely (usually the case), preventing any method from generating a highly accurate solution.

The other solution option (ISOLVC=0) uses an explicit finite difference approximation to Eqs. (4) and (5). The difference equations can be advanced either by (1) a simple one-step forward time update for transport involving advection, diffusion, dispersion, radioactive decay and equilibrium, reversible sorption, or (2) a fourth order Runge-Kutta solution for transport involving non-equilibrium, saturable and/or irreversible sorption. In either case two schemes are available for reducing or eliminating artificial diffusion introduced by the numerical methods, described below.

The finite difference forms of Eqs. (4) and (5) solved by TRACRN are

$$\frac{\partial S_\alpha}{\partial t} \approx \left[Q_{1\alpha} C_\alpha (S_{m\alpha} - S_\alpha) - Q_{2\alpha} S_\alpha (C_{0\alpha} - C_\alpha) + \lambda_{\alpha-1} \frac{S_{\alpha-1}}{M_{\alpha-1}} M_\alpha - \lambda_\alpha S_\alpha \right]_{ijk}^{(n)} \quad (62)$$

and

$$\begin{aligned} \frac{\partial C_\alpha}{\partial t} \approx & \left[\frac{J_\alpha}{\epsilon \rho_i^{n+1/2} \sigma_i^{n+1/2}} + \lambda_{\alpha-1} \frac{C_{\alpha-1}}{M_{\alpha-1}} M_\alpha - \left(\lambda_\alpha + \frac{1}{\sigma_i \rho_i} \right) \right. \\ & \left. \times \left(\frac{\partial \rho_i \sigma_i}{\partial t} \right) C_\alpha - \frac{\rho_m}{\epsilon (\sigma_i \rho_i)^{n+1/2}} \frac{\partial S_\alpha}{\partial t} \right]_{ijk}^{(n)} \quad (63) \end{aligned}$$

where ρ_i is density of the fluid carrying the tracer. This system of 2 · NTRCR ordinary differential equations is easily solved by a fourth-order Runge-Kutta method to provide $S_\alpha^{n+1}, C_\alpha^{n+1}, \alpha = 1, \dots, NTRCR$. Transport terms and chemical reaction terms are solved simultaneously.

For tracers carried in the liquid phase, Eqs. (62) and (63) should be approximately correct, even under partially saturated conditions. Water, a wetting fluid, will coat matrix

particles, so that even at low liquid saturations, binding sites and particles will be in contact with liquid. For airborne tracers, Eq. (62) may require modification because the sorption terms may not reflect the degree of contact between the gas phase and matrix grains for partially saturated conditions.

In Eq. (63), the flux term J_α is given by

$$J_\alpha = \sum_m \epsilon \sigma_i \left\{ D_\alpha \rho_i \frac{C_\alpha - C_{\alpha m}}{\Delta X_m} + [\bar{D}_\alpha \nabla(\rho_i C_\alpha)]_m \right\} \frac{\Delta A}{\Delta \Omega} (-1)^m - \sum_m \langle \rho_i C_\alpha \rangle_m (-1)^m \times \frac{u_{im}^{n+1}}{\Delta \Omega} \Delta A_m \quad (64)$$

The first summation on the right side of Eq. (64) is straightforward. The last term in Eq. (64) deserves comment. First, the velocities u_{im} are supplied by the flow part of the model. Second, the manner in which the tracer density at zone interfaces $\langle \rho_i C_\alpha \rangle_m$ is calculated can have a strong influence on the overall accuracy of the numerical solution. For example, a pure donor treatment of $\langle \rho_i C_\alpha \rangle_m$ would produce significant smearing of sharp concentration fronts (which typically occur for high Peclet number flows). The user has the option of specifying a donor type differencing scheme or a higher order method via input variable CDONOR.

The higher order representation used here for the $\langle \rho_i C_\alpha \rangle_m$ term at high Peclet number is fairly simple but appears to be capable of resolving sharp concentration fronts. It is similar to techniques that have recently appeared in the literature (Douglas and Russell 1982; Larson 1982). The flux term $\langle \rho_i C_\alpha \rangle_m$ is determined for each interface in three steps.

- (1) From \bar{u}_{im} , determine $\bar{x}_m = \bar{x}_m - \frac{\bar{u}_{im} \Delta t}{\epsilon}$.
- (2) Determine shape of the concentration front. If local Peclet number $Pe < 100$, use an approximate polynomial fit. If $Pe > 100$, use "sharp" donor approach [described in (2) below]

- (3) Integrate $\int_{\bar{x}_m}^{\bar{x}^*} \frac{\rho_i C_\alpha(\bar{x}) V_i(\bar{x})}{|x_m - \bar{x}_m|} d\bar{x}$ to obtain $\langle \rho_i C_\alpha \rangle_m u_{im}$.

For one-dimensional transport, this is easy to describe. Figure 6 shows a typical, large Peclet number concentration profile superimposed on a finite difference mesh. Consider the flux across the interface at x_R . The three steps for this instance are listed below.

- (1) Calculate $\bar{x} = x_R - V_R \Delta t$.
- (2) Determine $Pe = \frac{LV_R}{D}$. If $Pe < 100$, use a polynomial fit for C between x_L and x_R . If $Pe > 100$ and if $C_L > C > C_R$ or $C_L < C < C_R$, determine x_C from $C_L(x_C - x_L) + C_R(x_R - x_C) = C(x_R - x_L)$.
- (3) Then integrate $\int_{\bar{x}}^{x_R} \frac{\rho_i C_\alpha(x) V_i(x)}{|x_R - \bar{x}|} dx$ to obtain $\langle \rho_i C_\alpha \rangle_R u_R$.

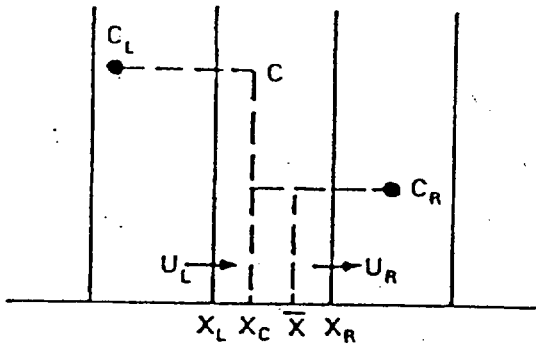


Fig. 6. Sharp donor scheme for high Peclet number 1-dimensional transport.

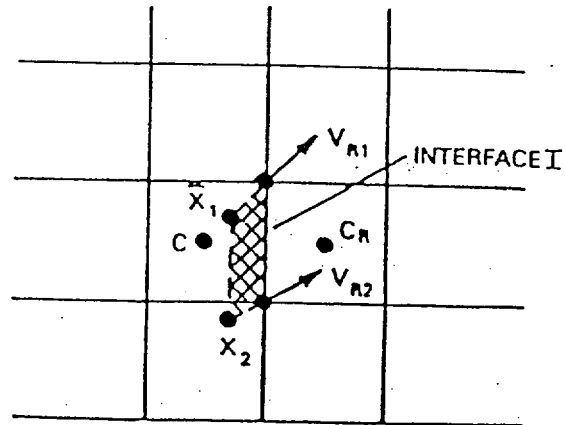


Fig. 7. Sharp donor scheme for high Peclet number 2-dimensional transport.

If $Pe > 100$ but $C_L > C > C_R$ or $C_L < C < C_R$ is not true, just use simple donor differencing.

For two- and three-dimensional problems, steps (2) and (3) become more involved. Figure 7 shows a typical situation for two-dimensional transport. Velocities at the corners of cells are determined, and the shaded area is calculated. The shaded area is the region that will pass through interface I (shown in Fig. 7). The most difficult task here is to compute the shape of the concentration field in the shaded region. This is done by interpolating between neighboring cell values. Once again, a Peclet number is computed. If $Pe < 100$, a polynomial fit is used. If $Pe > 100$ and concentration is monotonically increasing or decreasing in the direction of flow, a "sharp" donor approach is used. Finally, the integration of step (3) is performed. In three dimensions, the bookkeeping becomes considerable, but accuracy is the reward.

Under the third transport solution option (ISOLVC=0, CDONOR=0.5), the numerical dispersion is calculated directly and subtracted out, thereby enhancing the accuracy of the numerical results. When CDONOR=0.5, the differencing of spatial derivatives is centered (as opposed to donor differencing which biases the difference towards upstream nodes).

Centered differencing is more accurate than donor differencing but often tends to be unstable. The source of this instability (determined by truncation error analysis) is the low order differencing of the time derivatives, which introduces a negative diffusion-like term. Donor-differencing methods stabilize by adding on more positive numerical diffusion to overcome the negative term arising from the low order time differencing. However, they rarely add on exactly the right amount to cancel the negative diffusion, thereby

guaranteeing that there will be too much numerical diffusion. Rather than using a donor-type spatial differencing to offset the time truncation negative diffusion term, we estimate directly the magnitude of the time truncation term and subtract it for each mesh cell at each time step. (We could use a higher order differencing for the time derivative, but this would increase memory storage requirements.) This is illustrated for the case of transport in a saturated, homogeneous medium with steady uniform water flow. The procedure is identical for the more general cases.

The transport equation, then, is

$$\frac{\partial C}{\partial t} + \nabla \cdot (uC) = D\nabla^2 C \quad (65)$$

and our finite difference form is

$$\frac{C_i^{n+1} - C_i^n}{\Delta t} + \frac{u}{2} \sum_{q=1}^6 (C_i + C_{i+q}) \Delta A_q (-1)^q = D \sum_{q=1}^6 (C_{i+q} - C_i) \frac{\Delta A_q}{\Delta x_q} \quad (66)$$

To determine the truncation error, we expand terms in Eq. (66) in a Taylor series around C_i^n

$$\left[\frac{\partial C}{\partial t} \right]^n + \frac{\Delta t}{2} \left[\frac{\partial^2 C}{\partial t^2} \right]^n + [\nabla \cdot (uC)]^n + O(\Delta x^2, \Delta t^2) = D [\nabla^2 C]^n \quad (67)$$

So, to lowest order the differential equation that our difference equation (66) is approximating is not Eq. (65) but actually

$$\frac{\partial C}{\partial t} + \nabla \cdot (uC) = D\nabla^2 C - \frac{\Delta t}{2} \left(\frac{\partial^2 C}{\partial t^2} \right) \quad (68)$$

which approaches Eq. (65) as $\Delta t \rightarrow 0$. To estimate the last term in Eq. (68), we differentiate Eq. (65) to get

$$\begin{aligned} \frac{\partial^2 C}{\partial t^2} &= -\nabla \cdot \left(u \frac{\partial C}{\partial t} \right) + D\nabla^2 \frac{\partial C}{\partial t} \\ &\approx -\nabla \cdot u (-\nabla \cdot uC + D\nabla^2 C) \\ &\approx \nabla \cdot [u \nabla \cdot (uC)] \end{aligned} \quad (69)$$

which we then substitute into (68) to get

$$\frac{\partial C}{\partial t} + \nabla \cdot (\bar{u}C) = D\nabla^2 C - \frac{\Delta t}{2} \nabla \cdot [u \cdot (\nabla \cdot uC)] \quad (70)$$

To remove the artificial, and destabilizing, diffusion term in Eq. (70) we simply add that same term to our finite difference Eq. (66) to obtain

$$\begin{aligned} \frac{C_i^{n+1} - C_i^n}{\Delta t} + \frac{u}{2} \sum_{q=1}^6 (C_i + C_{i+q})^n \Delta A_q (-1)^q \\ = D \sum_{q=1}^6 (C_{i+q} - C_i)^n \frac{\Delta A_q}{\Delta x_q} + \frac{\Delta t}{2} u^2 \sum_{q=1}^6 (C_{i+q} - C_i)^n \frac{\Delta A_q}{\Delta x_q} \end{aligned} \quad (71)$$

This is our final finite difference form. Because of the form of Eq. (69), this approach is called TAD for tensor anti-diffusion. Equation (71) is now accurate to $O(\Delta t^2, \Delta x^2)$.

REFERENCES

- Bear, J. *Dynamics of Fluids in Porous Media* (American Elsevier Publishing Co., New York, 1972).
- Behie, A., and P. K. W. Vinsome, "Block Iterative Methods for Fully Implicit Reservoir Simulations," *Soc. Pet. Eng. J.*, 658-668 (1982).
- Brooks, R. H., and A. T. Corey, "Hydraulic Properties of Porous Media," *Hydrology Papers*, Colorado State University, Fort Collins, Colorado (1964).
- Diaz, J. C., W. R. Jines, and T. Sterhang, "On the Convergence Criteria for Linear (Inner) Iterative Solvers," *Eighth SPE Symposium on Reservoir Simulations*, Dallas, Texas, February 1985.
- Dullien, F. A. L., *Porous Media - Fluid Transport and Pore Structure* (Academic Press, New York, 1979), pp. 194-197.
- Douglas, J., Jr., and T. F. Russell, "Numerical Methods for Convection - Dominated Diffusion Problems Based on Combining the Method of Characteristics with Finite Element or Finite Difference Procedures," *SIAM J. Numer. Anal.* 19, No. 5, 871-885 (1982).
- Gelhar, L. W., "Stochastic Subsurface Hydrology From Theory to Applications," *Water Resources Research*, 22, 9, 135S-145S(1986).
- HISTORIANTM PLUS Reference Manual, Copyright 1985, by OPCODE, INC.
- Larson, R. G., "Controlling Numerical Dispersion by Variably Timed Flux Updating in Two Dimensions," *SPE J.*, pp. 409-419 (1982).
- Meijerink, J. A., and H. A. Van der Vorst, "An Iterative Solution Method for Linear Systems of Which the Coefficient Matrix is a Symmetric M-Matrix," *Mathematics of Computation* 31, 148-162 (1981).
- Mualem, Y., "A New Model for Predicting the Hydraulic Conductivity of Unsaturated Porous Materials," *Water Resources Research* 12, 3, 513-522 (1976).
- Perkins, B., B. J. Travis, and G. DePoorter, "Validation of the TRACR3D Code for Soil Water Flow Under Saturated/Unsaturated Conditions in Three Experiments," Los Alamos National Laboratory report LA-10263-MS (1985).
- Pigford, T. H., P. L. Chambré, M. Albert, M. Foglia, M. Harada, F. Iwamoto, T. Kanki, D. Leung, S. Masuda, S. Muraoka, and D. Ting, "Migration of Radio-Nuclides Through Sorbing Media Analytical Solutions-II," Lawrence Berkeley Laboratory report LBL-11616 (1980).

Polzer, W. L., H. R. Fuentes, E. P. Springer, and J. W. Nyhan, "Modeling Study of Solute Transport in the Unsaturated Zone," Vol. 1, Los Alamos National Laboratory, NUREG/CR-4615-V1, LA-10730-MS (1986).

Travis, B. J., "TRACR3D: A Model of Flow and Transport in Porous/Fractured Media," Los Alamos National Laboratory report LA-9667-MS (1984).

Travis, B. J., and H. E. Nuttall, "Two-Dimensional Numerical Simulation of Geochemical Transport in Yucca Mountain," Los Alamos National Laboratory report LA-10532-MS, (1987).

Van Genuchten, R., "Calculating the Unsaturated Hydraulic Conductivity with a New Closed Form Analytical Model," *Water Resources Bulletin*, Princeton University Press, Princeton University, Princeton, NJ. (1978).

Wolfe, J., and G. Zyzolowski, "Comparison of Reordering Schemes in Incomplete Factorization Methods," Los Alamos National Laboratory document LA-UR-86-2527 (1986).

Zyzolowski, G., "Incomplete Factorization for Finite Element Methods," *International Journal for Numerical Methods in Engineering*, 23, 1101-1109 (1986).